Cluster Cosmology Constraints from the 2500 deg2 SPT-SZ Survey: Inclusion of Weak Gravitational Lensing Data from Magellan and the Hubble Space Telescope

Item Type	Article
Authors	Bocquet, S.; Dietrich, J. P.; Schrabback, T.; Bleem, L. E.; Klein, M.; Allen, S. W.; Applegate, D. E.; Ashby, M. L. N.; Bautz, M.; Bayliss, M.; Benson, B. A.; Brodwin, M.; Bulbul, E.; Canning, R. E. A.; Capasso, R.; Carlstrom, J. E.; Chang, C. L.; Chiu, I.; Cho, H-M.; Clocchiatti, A.; Crawford, T. M.; Crites, A. T.; Haan, T. de; Desai, S.; Dobbs, M. A.; Foley, R. J.; Forman, W. R.; Garmire, G. P.; George, E. M.; Gladders, M. D.; Gonzalez, A. H.; Grandis, S.; Gupta, N.; Halverson, N. W.; Hlavacek-Larrondo, J.; Hoekstra, H.; Holder, G. P.; Holzapfel, W. L.; Hou, Z.; Hrubes, J. D.; Huang, N.; Jones, C.; Khullar, G.; Knox, L.; Kraft, R.; Lee, A. T.; Linden, A. von der; Luong-Van, D.; Mantz, A.; Marrone, D. P.; McDonald, M.; McMahon, J. J.; Meyer, S. S.; Mocanu, L. M.; Mohr, J. J.; Morris, R. G.; Padin, S.; Patil, S.; Pryke, C.; Rapetti, D.; Reichardt, C. L.; Rest, A.; Ruhl, J. E.; Saliwanchik, B. R.; Saro, A.; Sayre, J. T.; Schaffer, K. K.; Shirokoff, E.; Stalder, B.; Stanford, S. A.; Staniszewski, Z.; Stark, A. A.; Story, K. T.; Strazzullo, V.; Stubbs, C. W.; Vanderlinde, K.; Vieira, J. D.; Vikhlinin, A.; Williamson, R.; Zenteno, A.
Citation	Bocquet, S., Dietrich, J. P., Schrabback, T., Bleem, L. E., Klein, M., Allen, S. W., … & Benson, B. A. (2019). Cluster Cosmology Constraints from the 2500 deg2 SPT-SZ Survey: Inclusion of Weak Gravitational Lensing Data from Magellan and the Hubble Space Telescope. The Astrophysical Journal, 878(1), 55.
DOI	10.3847/1538-4357/ab1f10
Publisher	IOP PUBLISHING LTD
Journal	ASTROPHYSICAL JOURNAL

Cluster Cosmology Constraints from the 2500 deg² SPT-SZ Survey: Inclusion of Weak Gravitational Lensing Data from Magellan and the *Hubble Space Telescope*

S. Bocquet[1,2,3], J. P. Dietrich[1,4], T. Schrabback[5], L. E. Bleem[2,3], M. Klein[1,6], S. W. Allen[7,8,9], D. E. Applegate[3], M. L. N. Ashby[10], M. Bautz[11], M. Bayliss[11], B. A. Benson[3,12,13], M. Brodwin[14], E. Bulbul[10], R. E. A. Canning[7,8], R. Capasso[1,4], J. E. Carlstrom[2,3,12,15,16], C. L. Chang[2,3,12], I. Chiu[17], H-M. Cho[18], A. Clocchiatti[19], T. M. Crawford[3,12], A. T. Crites[3,12,20], T. de Haan[21], S. Desai[22], M. A. Dobbs[23,24], R. J. Foley[25,26], W. R. Forman[10], G. P. Garmire[27], E. M. George[6,21], M. D. Gladders[3,12], A. H. Gonzalez[28], S. Grandis[1,4], N. Gupta[29], N. W. Halverson[30], J. Hlavacek-Larrondo[8,31,32], H. Hoekstra[33], G. P. Holder[23], W. L. Holzapfel[21], Z. Hou[3,15], J. D. Hrubes[34], N. Huang[21], C. Jones[10], G. Khullar[3,12], L. Knox[35], R. Kraft[10], A. T. Lee[21,36], A. von der Linden[37], D. Luong-Van[34], A. Mantz[7,8], D. P. Marrone[38], M. McDonald[11], J. J. McMahon[39], S. S. Meyer[3,12,15,16], L. M. Mocanu[3,12], J. J. Mohr[1,4,6], R. G. Morris[7,9], S. Padin[3,12,20], S. Patil[29], C. Pryke[40], D. Rapetti[1,4,30,41], C. L. Reichardt[29], A. Rest[42], J. E. Ruhl[43], B. R. Saliwanchik[44], A. Saro[1,4,45], J. T. Sayre[30], K. K. Schaffer[3,16,46], E. Shirokoff[3,12], B. Stalder[10], S. A. Stanford[35,47], Z. Staniszewski[43], A. A. Stark[10], K. T. Story[7,8], V. Strazzullo[1], C. W. Stubbs[10,48], K. Vanderlinde[49,50], J. D. Vieira[25,26], A. Vikhlinin[10], R. Williamson[3,12,20], and A. Zenteno[51]

[1] Faculty of Physics, Ludwig-Maximilians-Universität, Scheinerstr. 1, D-81679 Munich, Germany; sebastian.bocquet@physik.lmu.de
[2] HEP Division, Argonne National Laboratory, Argonne, IL 60439, USA
[3] Kavli Institute for Cosmological Physics, University of Chicago, Chicago, IL 60637, USA
[4] Excellence Cluster Universe, Boltzmannstr. 2, D-85748 Garching, Germany
[5] Argelander-Institut für Astronomie, Auf dem Hügel 71, D-53121 Bonn, Germany
[6] Max Planck Institute for Extraterrestrial Physics, Giessenbachstr. 1, D-85748 Garching, Germany
[7] Kavli Institute for Particle Astrophysics and Cosmology, Stanford University, 452 Lomita Mall, Stanford, CA 94305, USA
[8] Department of Physics, Stanford University, 382 Via Pueblo Mall, Stanford, CA 94305, USA
[9] SLAC National Accelerator Laboratory, 2575 Sand Hill Road, Menlo Park, CA 94025, USA
[10] Center for Astrophysics | Harvard & Smithsonian, Cambridge, MA 02138, USA
[11] Kavli Institute for Astrophysics and Space Research, Massachusetts Institute of Technology, 77 Massachusetts Avenue, Cambridge, MA 02139, USA
[12] Department of Astronomy and Astrophysics, University of Chicago, Chicago, IL 60637, USA
[13] Fermi National Accelerator Laboratory, Batavia, IL 60510-0500, USA
[14] Department of Physics and Astronomy, University of Missouri, 5110 Rockhill Road, Kansas City, MO 64110, USA
[15] Department of Physics, University of Chicago, Chicago, IL 60637, USA
[16] Enrico Fermi Institute, University of Chicago, Chicago, IL 60637, USA
[17] Institute of Astronomy and Astrophysics, Academia Sinica, Taipei 10617, Taiwan
[18] NIST Quantum Devices Group, Boulder, CO 80305, USA
[19] Departamento de Astronomia y Astrosifica, Pontificia Universidad Catolica, Chile
[20] California Institute of Technology, Pasadena, CA 91125, USA
[21] Department of Physics, University of California, Berkeley, CA 94720, USA
[22] Department of Physics, IIT Hyderabad, Kandi, Telangana 502285, India
[23] Department of Physics, McGill University, Montreal, QC H3A 2T8, Canada
[24] Canadian Institute for Advanced Research, CIFAR Program in Cosmology and Gravity, Toronto, ON M5G 1Z8, Canada
[25] Astronomy Department, University of Illinois at Urbana-Champaign, 1002 W. Green Street, Urbana, IL 61801, USA
[26] Department of Physics, University of Illinois Urbana-Champaign, 1110 W. Green Street, Urbana, IL 61801, USA
[27] Huntingdon Institute for X-ray Astronomy, LLC, USA
[28] Department of Astronomy, University of Florida, Gainesville, FL 32611, USA
[29] School of Physics, University of Melbourne, Parkville, VIC 3010, Australia
[30] Department of Astrophysical and Planetary Sciences and Department of Physics, University of Colorado, Boulder, CO 80309, USA
[31] Department of Physics, Université de Montréal, Montreal, QC H3T 1J4, Canada
[32] Kavli Institute for Particle Astrophysics and Cosmology, Stanford University, 452 Lomita Mall, Stanford, CA 94305-4085, USA
[33] Leiden Observatory, Leiden University, Niels Bohrweg 2, 2333 CA, Leiden, the Netherlands
[34] University of Chicago, Chicago, IL 60637, USA
[35] Department of Physics, University of California, Davis, CA 95616, USA
[36] Physics Division, Lawrence Berkeley National Laboratory, Berkeley, CA 94720, USA
[37] Department of Physics and Astronomy, Stony Brook University, Stony Brook, NY 11794, USA
[38] Steward Observatory, University of Arizona, 933 North Cherry Avenue, Tucson, AZ 85721, USA
[39] Department of Physics, University of Michigan, Ann Arbor, MI 48109, USA
[40] Department of Physics, University of Minnesota, Minneapolis, MN 55455, USA
[41] NASA Ames Research Center, Moffett Field, CA 94035, USA
[42] Space Telescope Science Institute, 3700 San Martin Dr., Baltimore, MD 21218, USA
[43] Physics Department, Center for Education and Research in Cosmology and Astrophysics, Case Western Reserve University, Cleveland, OH 44106, USA
[44] Department of Physics, Yale University, New Haven, CT 06511, USA
[45] INAF-Osservatorio Astronomico di Trieste, via G.B. Tiepolo 11, I-34143 Trieste, Italy
[46] Liberal Arts Department, School of the Art Institute of Chicago, Chicago, IL 60603, USA
[47] Institute of Geophysics and Planetary Physics, Lawrence Livermore National Laboratory, Livermore, CA 94551, USA
[48] Department of Physics, Harvard University, 17 Oxford Street, Cambridge, MA 02138, USA
[49] Dunlap Institute for Astronomy & Astrophysics, University of Toronto, 50 St George St., Toronto, ON, M5S 3H4, Canada
[50] Department of Astronomy & Astrophysics, University of Toronto, 50 St George St., Toronto, ON, M5S 3H4, Canada
[51] Cerro Tololo Inter-American Observatory, Casilla 603, La Serena, Chile

Abstract

We derive cosmological constraints using a galaxy cluster sample selected from the 2500 deg^2 SPT-SZ survey. The sample spans the redshift range $0.25 < z < 1.75$ and contains 343 clusters with SZ detection significance $\xi > 5$. The sample is supplemented with optical weak gravitational lensing measurements of 32 clusters with $0.29 < z < 1.13$ (from Magellan and *Hubble Space Telescope*) and X-ray measurements of 89 clusters with $0.25 < z < 1.75$ (from *Chandra*). We rely on minimal modeling assumptions: (i) weak lensing provides an accurate means of measuring halo masses, (ii) the mean SZ and X-ray observables are related to the true halo mass through power-law relations in mass and dimensionless Hubble parameter $E(z)$ with a priori unknown parameters, and (iii) there is (correlated, lognormal) intrinsic scatter and measurement noise relating these observables to their mean relations. We simultaneously fit for these astrophysical modeling parameters and for cosmology. Assuming a flat $\nu\Lambda$CDM model, in which the sum of neutrino masses is a free parameter, we measure $\Omega_m = 0.276 \pm 0.047$, $\sigma_8 = 0.781 \pm 0.037$, and $\sigma_8(\Omega_m/0.3)^{0.2} = 0.766 \pm 0.025$. The redshift evolutions of the X-ray Y_X–mass and M_{gas}–mass relations are both consistent with self-similar evolution to within 1σ. The mass slope of the Y_X–mass relation shows a 2.3σ deviation from self-similarity. Similarly, the mass slope of the M_{gas}–mass relation is steeper than self-similarity at the 2.5σ level. In a νwCDM cosmology, we measure the dark energy equation-of-state parameter $w = -1.55 \pm 0.41$ from the cluster data. We perform a measurement of the growth of structure since redshift $z \sim 1.7$ and find no evidence for tension with the prediction from general relativity. This is the first analysis of the SPT cluster sample that uses direct weak-lensing mass calibration and is a step toward using the much larger weak-lensing data set from DES. We provide updated redshift and mass estimates for the SPT sample.

Key words: cosmological parameters – cosmology: observations – galaxies: clusters: general – large-scale structure of universe

Supporting material: machine-readable table

1. Introduction

Measurements of the abundance of galaxy clusters have become an important part of the cosmological toolkit. Galaxy clusters and their associated dark matter halos trace the highest and therefore rarest peaks in the matter density field on megaparsec scales. To obtain cosmological constraints, one confronts the predicted halo abundance, the halo mass function (HMF), which is provided by numerical cosmological simulations, with the observations. The key challenge is to accurately describe the relation between halo mass in the simulations and the observable quantities. The cluster abundance essentially constrains the parameter combination $\sigma_8(\Omega_m/0.3)^{\alpha}$, where σ_8 is the rms fluctuation in the linear matter density field on $8\,\mathrm{Mpc}/h$ scales at $z = 0$ and α is of the order of about 0.2–0.4 depending on survey specifics. Measuring the cluster abundance over a range of redshifts enables constraints on the cosmic expansion and structure formation histories. This probe can therefore be used to challenge the paradigms of a cosmological constant and of general relativity and, when analyzed jointly with measurements of primary anisotropies in the cosmic microwave background (CMB), to measure the sum of neutrino masses (for reviews, see, e.g., Allen et al. 2011; Kravtsov & Borgani 2012).

Cosmological analyses have been performed using samples of galaxy clusters constructed from their observed galaxy populations (e.g., Rykoff et al. 2016), their X-ray emission (e.g., Vikhlinin et al. 2009b; Mantz et al. 2010b), and their millimeter-wave signal (e.g., Bleem et al. 2015; Planck Collaboration et al. 2016b; Hilton et al. 2018). The latter is dominated by the thermal Sunyaev–Zel'dovich effect (SZ; Sunyaev & Zel'dovich 1972), which arises when CMB photons scatter off hot electrons in the intracluster medium (ICM). The surface brightness of the SZ effect is independent of cluster redshift, and high-resolution millimeter-wave surveys can therefore be used to construct clean and essentially mass-limited catalogs out to the highest redshifts at which clusters exist. This makes SZ-selected cluster samples particularly suited for studying the evolution of scaling relations and the growth of cosmic structure over a significant fraction of the age of the universe.

In this paper, we present an analysis of the 2500 deg^2 SPT-SZ survey cluster sample that is enabled by optical weak gravitational lensing (WL) data for SPT-SZ clusters. The WL data set consists of two subsamples: (i) 19 clusters at intermediate redshifts $0.28 < z < 0.63$, with ground-based Magellan/Megacam imaging, referred to as the "Megacam sample" hereafter (Dietrich et al. 2019, hereafter D19); and (ii) 13 clusters at higher redshifts $0.58 < z < 1.13$ observed with the *Hubble Space Telescope* (*HST*), referred to as the "*HST* sample" hereafter (Schrabback et al. 2018a, hereafter S18). Using these WL data in our analysis has two main advantages: (i) it removes the need to rely on external calibrations of the observable–mass relations, and (ii) our analysis now only considers clusters that are actually part of the SPT-SZ sample, which ensures a fully self-consistent handling of selection effects.

This work represents an improvement over the first cosmological analysis of the SZ-selected cluster sample from the full 2500 deg^2 SPT-SZ survey (de Haan et al. 2016, hereafter dH16), where we combined the cluster number counts in SZ significance and redshift with X-ray Y_X follow-up (Y_X is the product of X-ray gas mass M_{gas} and temperature T_X; Kravtsov et al. 2006) of 82 clusters. The dH16 analysis relied on external, WL-based calibrations of the normalization of the Y_X–mass relation and the assumption that its evolution in mass and redshift follows the self-similar expectation within some uncertainty (5% and 50% uncertainty at 1σ on the parameters of the mass and redshift evolution, respectively).

As already mentioned, the key challenge in cluster cosmology is to robustly model the relation between the observables (SZ signal, WL shear profiles, X-ray Y_X measurements) and the underlying, unobserved halo mass, which is the link to the predicted HMF.[52] Our modeling assumptions are as follows:

---

[52] Although some of the observables carry cosmological dependences themselves, we seek to constrain cosmology primarily through its impact on the HMF.

1. The relation between true halo mass and the observed WL signal and the scatter around this mean relation are well understood, with systematic uncertainties at the few percent level. We use numerical simulations to account for the effects of halo triaxiality, miscentering, and correlated large-scale structure along the line of sight. Uncorrelated large-scale structure along the line of sight is accounted for in a semianalytic approach (Megacam sample) and via simulated cosmic shear fields (*HST* sample). For the Megacam sample, the systematic limit in mass is 5.6% (D19), and it is 9.2%–9.4% for the *HST* sample (S18).

2. The mean relations between true halo mass and the SZ and X-ray observables are described by power-law relations in mass and the dimensionless Hubble parameter $E(z) \equiv H(z)/H_0$. This functional form is motivated by the self-similar model (evolution assuming that only gravity is at play; Kaiser 1986) and confirmed using numerical *N*-body and hydrodynamical simulations (e.g., Vanderlinde et al. 2010; de Haan et al. 2016; Gupta et al. 2017a). However, we do not assume any a priori knowledge of the parameters in these relations and allow for departures from self-similarity by marginalizing over wide priors.

3. The intrinsic scatter in the SZ and X-ray observable–mass relations is described by lognormal distributions (with a priori unknown width). The scatter among all three observables may be correlated, and we marginalize over the correlation coefficients.

This paper is organized as follows: In Section 2, we provide an overview of the cluster data set and of external cosmological data used in the analysis. We describe our analysis method in Section 3. In Section 4, we present our constraints on scaling relations and cosmology. We summarize our findings in Section 5 and provide some outlook. Further robustness tests are discussed in Appendices A–C.

Throughout this work we assume spatially flat cosmological models. Cluster masses are referred to as $M_{\Delta c}$, the mass enclosed within a sphere of radius r_Δ, in which the mean matter density is equal to Δ times the critical density. The critical density at the cluster's redshift is $\rho_{\rm crit}(z) = 3H^2(z)/8\pi G$, where $H(z)$ is the Hubble parameter. We refer to the vector of cosmology and scaling relation parameters as $\boldsymbol{p}$.

All quoted constraints correspond to the mean and the shortest 68% credible interval, computed from the MCMC chains using a Gaussian kernel density estimator.[53] All multidimensional posterior probability plots show the 68% and 95% contours. We use standard notation for statistical distributions, i.e., the normal distribution with mean $\boldsymbol{\mu}$ and covariance matrix $\boldsymbol{\Sigma}$ is written as $\mathcal{N}(\boldsymbol{\mu}, \boldsymbol{\Sigma})$, and $\mathcal{U}(a, b)$ denotes the uniform distribution on the interval $[a, b]$.

2. Data

The cluster cosmology sample from the 2500 deg^2 SPT-SZ survey consists of 365 candidates, of which 343 are optically confirmed and have redshift measurements. X-ray follow-up measurements with *Chandra* are available for 89 clusters, and WL shear profiles are available for 19 clusters from ground-based observations with Magellan/Megacam and for 13 clusters observed from space with *HST* (see Figure 1).
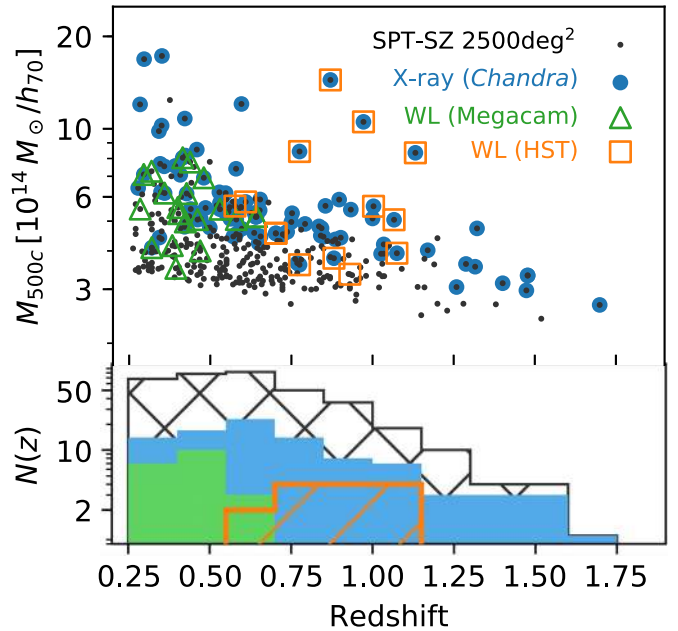

Figure 1. SPT-SZ 2500 deg^2 cluster cosmology sample, selected to have redshift $z > 0.25$ and detection significance $\xi > 5$. Top panel: distribution of clusters in redshift and mass (assuming a fiducial observable–mass relation). Black circles show the full sample, blue circles mark those 89 clusters for which X-ray follow-up data from *Chandra* are available, and green triangles (orange squares) mark those 19 with Magellan/Megacam (13 with *HST*) WL follow-up data. Bottom panel: histograms with the same color-coding. While the X-ray follow-up data set covers the entire redshift range, the WL follow-up covers $0.25 < z \lesssim 1.1$.

2.1. The SPT-SZ 2500 deg^2 Cluster Sample

The South Pole Telescope (SPT) is a 10 m telescope located within 1 km of the geographical South Pole (Carlstrom et al. 2011). The $\sim 1'$ resolution and $1°$ field of view are well suited for a survey of rare, high-mass clusters from a redshift of $z \geqslant 0.2$ out to the highest redshifts where they exist. From 2007 to 2011, the telescope was configured to observe with the SPT-SZ camera in three millimeter-wave bands (centered at 95, 150, and 220 GHz). The majority of this period was spent on the SPT-SZ survey, a contiguous 2500 deg^2 area within the boundaries $20^{\rm h} \leqslant$ R.A. $\leqslant 7^{\rm h}$ and $-65° \leqslant$ decl. $\leqslant -40°$. The survey achieved a fiducial depth of $\leqslant 18\,\mu$K arcmin in the 150 GHz band.

Galaxy clusters are detected via their thermal SZ signature in the 95 and 150 GHz maps. These maps are created using time-ordered data processing and map-making procedures equivalent to those described in Vanderlinde et al. (2010) and Reichardt et al. (2013). Galaxy clusters are extracted using a multiscale matched-filter approach (Melin et al. 2006) applied to the multiband data as described in Williamson et al. (2011) and Reichardt et al. (2013).

We use the same SPT-SZ cluster sample that was analyzed in dH16. Namely, this *cosmological sample* is a subset of the full SPT-SZ cluster sample presented in Bleem et al. (2015), restricted to redshifts $z > 0.25$ and detection significances $\xi > 5$. This cosmological sample has an expected and measured purity of 95% (Bleem et al. 2015). For clusters at redshifts below $z = 0.25$, confusion with primary CMB fluctuations changes the scaling of the ξ–mass relation.

We have improved the cluster redshift estimates from the original values provided in Bleem et al. (2015) to incorporate

new spectroscopic measurements (Bayliss et al. 2016; Khullar et al. 2019; A. Mantz et al. 2019, in preparation), two updated high-redshift photo-z measurements with *HST* (Strazzullo et al. 2019), and improved photometric measurements. These improved photometric redshifts are enabled both via the recalibration of our *Spitzer* redshift models using the new spectroscopic data and by the use of optical data from the Parallel Imager for Southern Cosmology Observations (PISCO), a new imager installed on the Magellan/Clay telescope at Las Campanas Observatory (Stalder et al. 2014). PISCO—with a fast (∼20 s) readout, 9′ field of view, and simultaneous four-band (*griz*) imaging capability—is optimized for efficient characterization of clusters and other systems identified from external surveys. As part of further efforts to characterize the SPT-SZ cluster sample, we have obtained approximately uniform PISCO imaging for the majority of the previously confirmed SPT-SZ clusters. Notably, these deeper optical data have allowed less constraining infrared-driven redshift estimates from *Spitzer* to be replaced by more robust estimates based on optical red sequence techniques for a significant number of clusters in the range $0.8 \lesssim z \lesssim 1$. As a consequence, while the improved data and model calibration result in small changes in redshift estimates for systems at $z \lesssim 0.8$ and $z \gtrsim 1$, at intermediate redshifts, replacing infrared-driven redshifts with more robust optical estimates leads to up to 1.5σ systematic shifts; see Figure 2. We will briefly come back to this issue in Section 4.3.

2.2. X-Ray Measurements

We use X-ray measurements for a subsample of 89 clusters. Eighty-one of these were also used in our previous cosmological analysis (dH16). We decided not to use the X-ray data available for SPT-CL J0142-5032 because of its large measurement error in temperature exceeding 40%. This has a negligible impact on our results. Most of those X-ray measurements were originally presented in McDonald et al. (2013), and they were largely acquired through a *Chandra* X-ray Visionary Project (PI: Benson). This sample is now supplemented with observations of eight high-redshift $z > 1.2$ clusters (McDonald et al. 2017). We refer the reader to these references for the details of the X-ray analysis.

The X-ray data products entering this analysis are (i) lookup tables of the total gas mass, M_{gas}, within an outer radius ranging from 80 to 2000 kpc (calculated using a fiducial cosmology), allowing interpolation of M_{gas} within any realistic value of r_{500}; and (ii) spectroscopic temperatures, T_X, in the $0.15 r_{500}$–$1.0 r_{500}$ aperture. All X-ray measurements were remade for this work using the *Chandra* calibration CALDB v4.7.7. Note that this calibration does not change the results from dH16.

2.3. Weak Gravitational Lensing Data

We use WL measurement for 32 clusters in our sample. Of these, 19 were observed with Magellan/Megacam at redshifts $0.29 \leqslant z \leqslant 0.69$ (D19), and 13 at redshifts $0.576 \leqslant z \leqslant 1.132$ with the Advanced Camera for Surveys on board *HST* (S18). Details on the data reduction and analysis methods can be found in these works.

The data products from these works used in our analysis are the reduced tangential shear profiles in angular coordinates, corrected for contamination by cluster galaxies, and the estimated redshift distributions of the selected source galaxies.
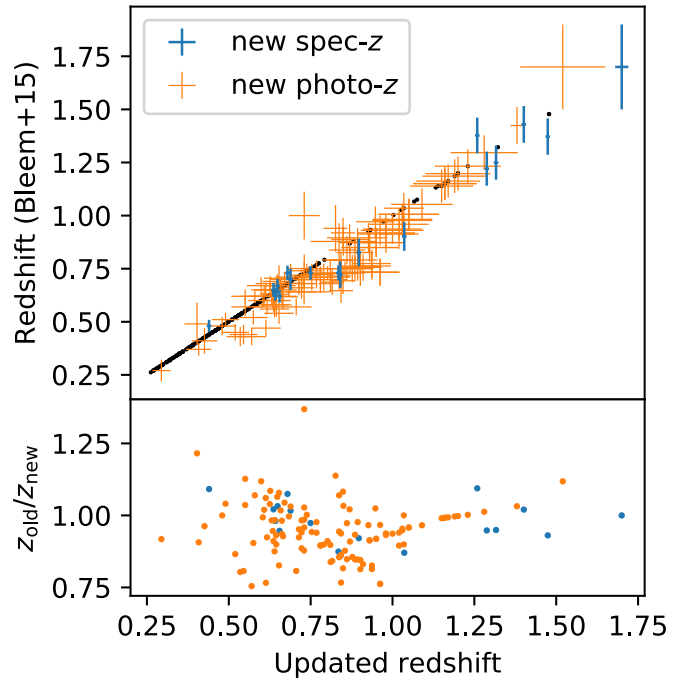

Figure 2. Updates in cluster redshifts since the publication of the SPT-SZ cluster catalog (Bleem et al. 2015). Top panel: original redshifts plotted against the updated ones. Black circles show unchanged redshifts (without error bars for ease of presentation), orange error bars show updated photometric redshifts, and blue error bars show new spectroscopic measurements. Bottom panel: changes in redshifts; we omit unchanged redshifts and all error bars. Orange circles show the change in photo-z values, and blue circles show changes due to new spec-z measurements.

These are the observable quantities, which are independent from cosmology, whereas mass estimates or shear profiles in physical coordinates depend on cosmology through the redshift–distance relation and the cosmology dependence of the NFW profile. Our approach ensures a clean separation between the actual measurements and their modeling.

2.4. External Cosmological Data Sets

In addition to our cluster data set, we will also consider external cosmological probes. We use measurements of primary CMB anisotropies from *Planck* and focus on the TT +lowTEB data combination from the 2015 analysis (Planck Collaboration et al. 2016a). We use angular diameter distances as probed by baryon acoustic oscillations (BAOs) by the 6dF Galaxy Survey (Beutler et al. 2011), the SDSS Data Release 7 Main Galaxy Sample (Ross et al. 2015), and the BOSS Data Release 12 (Alam et al. 2017). We also use measurements of luminosity distances from Type Ia supernovae (SNe Ia) from the Pantheon sample (Scolnic et al. 2018).

3. Analysis Method

In this section, we present the observable–mass relations, the likelihood function, and the priors adopted. Figure 3 shows a flowchart of the analysis pipeline. The data and likelihood code will be made publicly available.

3.1. Observable–Mass Relations

We consider three cluster mass proxies: the unbiased SZ significance ζ, the X-ray Y_X, and the WL mass M_{WL}. We
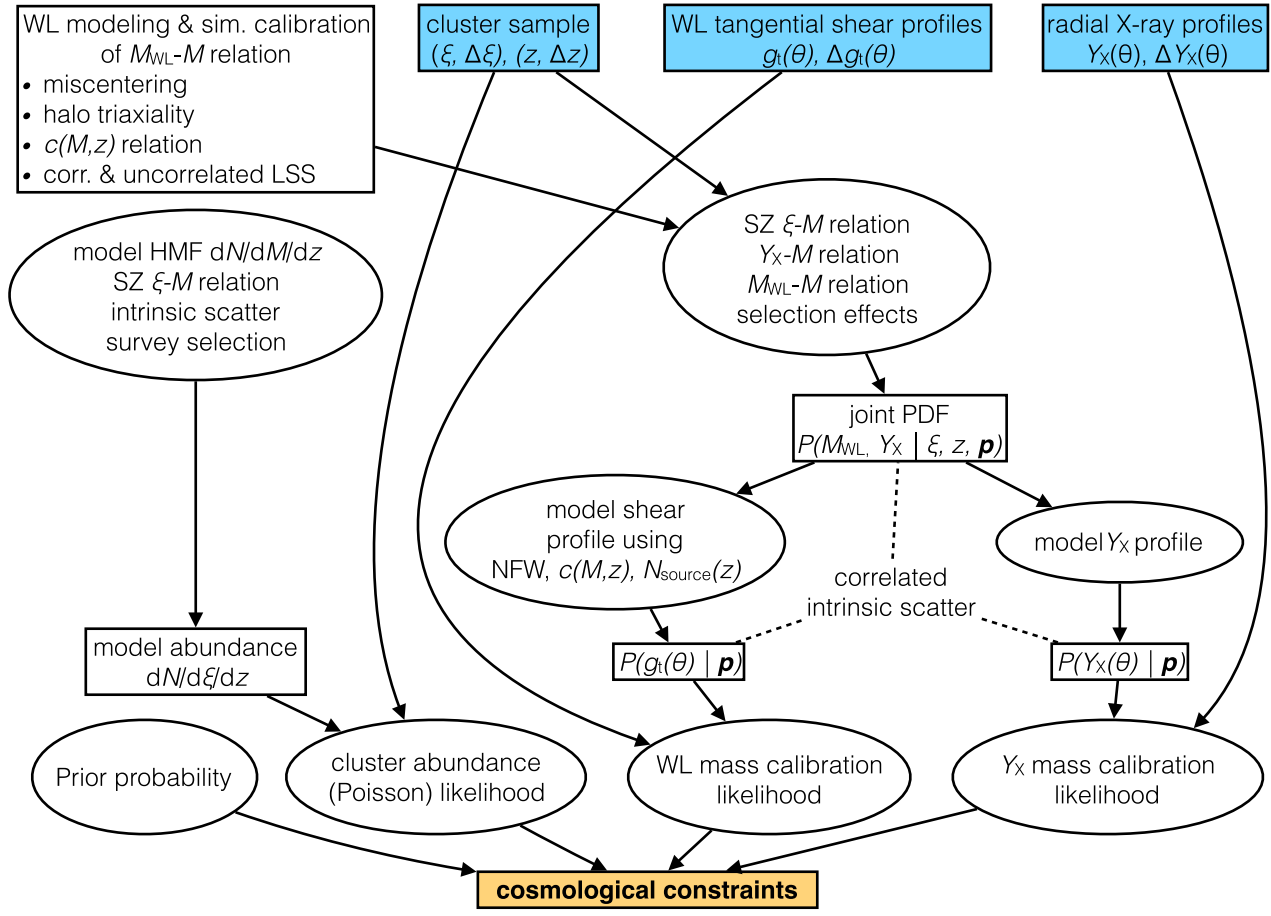
Figure 3. Analysis flowchart showing how the cluster data (blue boxes) are used to obtain cosmological constraints (orange box). White boxes show model predictions, and ellipses show functions that use or create those models. The number count analysis is performed using the full SPT-SZ catalog, while the mass calibration is performed using the subset of clusters for which follow-up data are available.

parameterize the mean observable–mass relations as

$$\langle \ln \zeta \rangle = \ln A_{SZ} \; + B_{SZ} \, \ln \left(\frac{M_{500c} \, h_{70}}{4.3 \, \times \, 10^{14} M_\odot} \right)$$
$$+ \; C_{SZ} \, \ln \left(\frac{E(z)}{E(0.6)} \right) \tag{1}$$

$$\ln \left(\frac{M_{500c} \, h_{70}}{8.37 \, \times \, 10^{13} M_\odot} \right) = \ln A_{Y_X} \; + B_{Y_X} \langle \ln Y_X \rangle$$
$$+ \; B_{Y_X} \ln \left(\frac{h_{70}^{5/2}}{3 \, \times \, 10^{14} M_\odot \mathrm{keV}} \right)$$
$$+ \; C_{Y_X} \ln E(z) \tag{2}$$

$$\langle \ln M_{WL} \rangle = \ln b_{WL} + \ln M_{500c}. \tag{3}$$

The ζ–mass and Y_X–mass relations are equivalent to the ones adopted in dH16, except for replacing $h/0.72$ by h_{70} in Y_X–mass.

The intrinsic scatter in $\ln \zeta$, $\ln Y_X$, and $\ln M_{WL}$ at fixed mass and redshift is described by normal distributions with widths $\sigma_{\ln \zeta}$, $\sigma_{\ln Y_X}$, and σ_{WL}. These widths are assumed to be independent of mass and redshift. Note that the parameters $\sigma_{\ln \zeta}$ and $\sigma_{\ln Y_X}$ have been called D_{SZ} and D_X in some previous SPT publications. We allow for correlated scatter between the SZ, X-ray, and WL mass proxies as described by the

covariance matrix

$$\boldsymbol{\Sigma}_{\text{multi-obs}}$$
$$= \begin{pmatrix} \sigma_{\ln \zeta}^2 & \rho_{SZ-WL}\sigma_{\ln \zeta}\sigma_{WL} & \rho_{SZ-X}\sigma_{\ln \zeta}\sigma_{\ln Y_X} \\ \rho_{SZ-WL}\sigma_{\ln \zeta}\sigma_{WL} & \sigma_{WL}^2 & \rho_{WL-X}\sigma_{WL}\sigma_{\ln Y_X} \\ \rho_{SZ-X}\sigma_{\ln \zeta}\sigma_{\ln Y_X} & \rho_{WL-X}\sigma_{WL}\sigma_{\ln Y_X} & \sigma_{\ln Y_X}^2 \end{pmatrix}$$
$$\tag{4}$$

with correlation coefficients ρ_{SZ-X}, ρ_{SZ-WL}, and ρ_{WL-X}. With this, the full description of the multi-observable–mass relation is

$$P \left(\begin{bmatrix} \ln \zeta \\ \ln M_{WL} \\ \ln Y_X \end{bmatrix} \middle| M, z, \boldsymbol{p} \right)$$
$$= \mathcal{N} \left(\begin{bmatrix} \langle \ln \zeta \rangle (M, z, \boldsymbol{p}) \\ \langle \ln M_{WL} \rangle (M, z, \boldsymbol{p}) \\ \langle \ln Y_X \rangle (M, z, \boldsymbol{p}) \end{bmatrix}, \boldsymbol{\Sigma}_{\text{multi-obs}} \right). \tag{5}$$

All parameters of the observable–mass relations are listed in Table 2.

While our default X-ray observable is Y_X, we also consider the X-ray gas mass M_{gas}. Note that both observables share the same M_{gas} data, and so we do not use them simultaneously. We

define a relation for the gas mass fraction $f_{\rm gas} \equiv M_{\rm gas}/M_{500c}$,

$$\langle \ln f_{\rm gas} \rangle = \ln\left(\frac{A_{M_{\rm g}}}{h_{70}^{3/2}}\right) + (B_{M_{\rm g}} - 1)\ln\left(\frac{M_{500c}\, h_{70}}{5 \times 10^{14} M_\odot}\right)$$
$$+ C_{M_{\rm g}}\ln\left(\frac{E(z)}{E(0.6)}\right), \qquad (6)$$

with which the $M_{\rm gas}$–mass relation becomes

$$\left\langle \ln\left(\frac{M_{\rm gas}}{5 \times 10^{14} M_\odot}\right) \right\rangle = \ln\left(\frac{A_{M_{\rm g}}}{h_{70}^{5/2}}\right) + B_{M_{\rm g}}\ln\left(\frac{M_{500c}\, h_{70}}{5 \times 10^{14} M_\odot}\right)$$
$$+ C_{M_{\rm g}}\ln\left(\frac{E(z)}{E(0.6)}\right).$$

3.1.1. The SZ ξ–Mass Relation

The observable we use to describe the cluster SZ signal is ξ, the detection signal-to-noise ratio (S/N) maximized over all filter scales. To account for the impact of noise bias, the unbiased SZ significance ζ is introduced, which is the S/N at the true, underlying cluster position and filter scale (Vanderlinde et al. 2010). Following previous SPT work, ξ across many noise realizations is related to ζ as

$$P(\xi|\zeta) = \mathcal{N}(\sqrt{\zeta^2 + 3}\,, 1). \qquad (8)$$

In practice, we only map objects with $\zeta > 2$ to ξ using this relation, but the exact location of this cut has no impact on our results (see also dH16). The validity of this approach and of Equation (8) has been extensively tested and confirmed by analyzing simulated SPT observations of mock SZ maps (Vanderlinde et al. 2010).

The SPT-SZ survey consists of 19 fields that were observed to different depths. The varying noise levels only affect the normalization of the ζ–mass relation and leave $B_{\rm SZ}$, $C_{\rm SZ}$, and $\sigma_{\ln\zeta}$ effectively unchanged (dH16). In the analysis presented here, $A_{\rm SZ}$ is rescaled by a correction factor for each of the 19 fields, which then allows us to work with a single SZ observable–mass relation, given by Equation (1). The scaling factors $\gamma_{\rm field}$ can be found in Table 1 in dH16.

In a departure from previous SPT analyses, we do not apply informative (Gaussian) priors on the SZ scaling relation parameters. The self-calibration through fitting the cluster sample against the HMF (see, e.g., Majumdar & Mohr 2004), the constraint on the normalization of the observable–mass relations through our WL data, and the constraint on the SZ scatter through the X-ray data are strong enough to constrain all four SZ scaling relation parameters (in $\nu\Lambda$CDM; see Table 3). When not including the X-ray data in our fit, however, we apply a Gaussian prior $\sigma_{\ln\zeta} = 0.13 \pm 0.13$ as in dH16 (this constraint was extracted from mock observations of hydrodynamic simulations from Le Brun et al. 2014).

We discuss possible limitations in our description of the ξ–mass relation that would lead to systematic biases in the recovered cosmological constraints. Because of our empirical weak-lensing mass calibration and the parameterization of the SZ scaling relation by power laws and lognormal scatter with free parameters, any bias in the SZ–mass relation that can be described by a power law and/or lognormal scatter would only lead to parameter shifts in the SZ scaling relation but would not

affect cosmological parameter constraints. Therefore, important systematics would be from potential contaminants that would lead to an additional, non-lognormal scatter, a mass or redshift dependence in the scatter, or a redshift dependence of the mass slope.

A potential worry might be the dilution of the SZ signal by AGN activity and the presence of dusty star-forming galaxies in the cluster. Various studies have found that emission by dusty star-forming galaxies is negligible compared to the SZ signal (see, e.g., Lin et al. 2009; Sehgal et al. 2010; and the summary in Section 6.4 in Benson et al. 2013). Gupta et al. (2017b) measured the cluster radio luminosity function using an X-ray-selected cluster sample at $z \lesssim 0.7$ and concluded that radio sources obeying this luminosity function would not have a strong impact on the SZ signal. Only a few percent at most of the SPT-SZ clusters would host sufficiently bright radio sources for their SZ signal to drop below the selection threshold, and this is within the Poisson uncertainty of our sample. At higher redshifts, it has been previously measured that the radio fraction in optically selected clusters somewhat decreases at $z > 0.65$ (Gralla et al. 2011). This result is consistent with simulations of the microwave sky from Sehgal et al. (2010), which predicted that the amount of radio contamination in SZ surveys was either flat or falling at $z > 0.8$. Using tests against mocks, we find, for example, that to cause a shift in w by more than $\Delta(w) = -0.3$, the level of SZ contamination would have to be strong enough to remove more than $\sim 30\%$ of all cluster detections at redshifts $z \gtrsim 1$, which by far exceeds the measurement by Gupta et al. (2017b). In conclusion, none of the discussed sources of potential SZ cluster contamination have an impact that is strong enough to introduce large biases in our cosmological constraints.

Another approach to testing the robustness of the SZ observable–mass relation is to compare it with other cluster mass proxies and try to find deviations from the simple scaling relation model. Note that if such a deviation were found, it would be hard to discern which observable is behaving in an unexpected way, but importantly, one would learn that the multi-observable model needs an extension. At low and intermediate redshifts $z \lesssim 0.8$, comparisons with cluster samples selected through optical and X-ray methods have shown that the cluster populations can be described by power-law observable–mass scaling relations with lognormal intrinsic scatter (Vikhlinin et al. 2009a; Mantz et al. 2010a, 2016; Saro et al. 2015, 2017). At higher redshifts, the subset of the SPT-selected sample with available X-ray observations from *Chandra* and *XMM-Newton* exhibits scaling relations in X-ray $T_{\rm X}$, $Y_{\rm X}$, $M_{\rm gas}$, and $L_{\rm X}$, as well as in stellar mass galaxies, that are consistent with power-law relations in mass and redshift with lognormal intrinsic scatter (Chiu et al. 2016, 2018; Hennig et al. 2017; Bulbul et al. 2019). When a redshift-dependent mass slope parameter has been included in the analyses of these data sets, the parameter constraints have been statistically consistent with 0 in all cases (see Table 4 in Bulbul et al. 2019).

In conclusion, our description of the ξ–mass relation has been confirmed by various independent techniques, especially for redshifts $z \lesssim 1$. Note that these tests are harder to perform at higher redshifts, where non-SZ-selected samples are small and more challenging to characterize. Our expectation is that as the cluster sample grows larger and the mass calibration information improves we will be able to characterize the currently negligible departures from our scaling relation model.

At that point, we will need to extend our observable–mass relation to allow additional freedom.

3.1.2. The Weak-lensing Observable–Mass Relation

The WL modeling framework used in this work is introduced in D19, and we refer the reader to their Section 5.2 for details.

The WL observable is the reduced tangential shear profile $g_t(\theta)$, which can be analytically modeled from the halo mass M_{200c}, assuming an NFW halo profile and using the redshift distribution of source galaxies (Wright & Brainerd 2000). Miscentering, halo triaxiality, large-scale structure along the line of sight, and uncertainties in the concentration–mass relation introduce bias and/or scatter. As introduced in Equation (3), we assume a relation $\ln M_{WL} = \ln(b_{WL} M_{true})$ and use numerical simulations to calibrate the normalization b_{WL} and the scatter about the mean relation. Our WL data set consists of two subsamples (Megacam and *HST*) with different measurement and analysis schemes. We expect some systematics to be shared among the entire sample, while others will affect each subsample independently.

We model the WL bias as

$$
\begin{aligned}
b_{WL,i} = b_{WL\ mass,i} \\
+ \delta_{WL,bias}\ \Delta b_{WL\ mass\ model,i} \\
+ \delta_i\ \Delta b_{measurement\ systematics,i}, \\
i \in \{Megacam, HST\},
\end{aligned}
\tag{9}
$$

where $b_{WL\ mass}$ is the mean bias due to WL mass modeling, $\Delta b_{WL\ mass\ model}$ is the uncertainty on $b_{WL\ mass}$, and $\Delta b_{measurement\ systematics}$ is the systematic measurement uncertainty due to multiplicative shear bias and uncertainties in the determination of the source redshift distribution; $\delta_{WL,bias}$, $\delta_{Megacam}$, and δ_{HST} are free parameters in our likelihood. With this parameterization, we apply Gaussian priors $\mathcal{N}(0, 1)$ on the three fit parameters. The numerical values of the different components of the WL bias are given in Table 1.

The width of the (lognormal) scatter that is intrinsic to fitting WL shear profiles against NFW profiles is

$$
\begin{aligned}
\sigma_{WL,i} = \sigma_{intrinsic,i} + \delta_{WL,scatter}\ \Delta\sigma_{intrinsic,i}, \\
i \in \{Megacam, HST\},
\end{aligned}
\tag{10}
$$

where $\sigma_{intrinsic}$ and $\Delta\sigma_{intrinsic}$ are the mean intrinsic scatter and the error on the mean, respectively (given in Table 1); $\delta_{WL,scatter}$ is a free parameter in our likelihood on which we apply a Gaussian prior $\mathcal{N}(0, 1)$.

Finally, the width of the (normal) scatter due to uncorrelated large-scale structure is

$$
\begin{aligned}
\sigma_{WL,LSS,i} = \sigma_{LSS,i} + \delta_{WL,LSS,i}\ \Delta\sigma_{LSS,i}, \\
i \in \{Megacam, HST\},
\end{aligned}
\tag{11}
$$

with the mean scatter σ_{LSS} and the error on the mean $\Delta\sigma_{LSS}$ given in Table 1, and where we apply a Gaussian prior $\mathcal{N}(0, 1)$ on the fit parameters $\delta_{WL,LSS_{Megacam}}$ and $\delta_{WL,LSS_{HST}}$.

For reference, the total systematic error in the WL calibration is 5.6% for the Megacam sample (D19) and 9.2%–9.4% for the *HST* sample (S18). Given the small sample size of 19 and 13 clusters, our WL mass calibration is still dominated by statistical errors.

3.2. Likelihood Function

The analysis pipeline used in this work evolved from the code originally used in a previous SPT analysis (Bocquet et al. 2015). Since then, we have updated it to the full 2500 deg^2 survey, included the handling of WL data and the ability to account for correlated scatter among all observables, and modified the X-ray analysis (see Section 3.2.2). The pipeline is written as a module for COSMOSIS (Zuntz et al. 2015) and was also used for other WL scaling relation studies of SPT-SZ clusters (D19; Stern et al. 2019).

We start from a multi-observable Poisson log-likelihood

$$
\begin{aligned}
\ln \mathcal{L}(\boldsymbol{p}) = \sum_i \ln \frac{dN(\xi, Y_X, g_t, z|\boldsymbol{p})}{d\xi dY_X\ dg_t\ dz}|_{\xi_i, Y_{X_i}, g_{t_i}, z_i} \\
- \iint \iint d\xi\ dY_X dg_t\ dz \\
\times \left[\frac{dN(\xi, Y_X, g_t, z|\boldsymbol{p})}{d\xi dY_X\ dg_t dz} \Theta_s \right] \\
+ const,
\end{aligned}
\tag{12}
$$

where the sum runs over all clusters i in the sample, and Θ_s is the survey selection function; in our case $\Theta_s = \Theta(\xi > 5, z > 0.25)$.

As discussed in Bocquet et al. (2015) and explicitly shown in their Appendix, we rewrite the first term in Equation (12) as $P(Y_X, g_t|\xi_i, z_i, \boldsymbol{p})|_{Y_{X_i}, g_{t_i}} \times \frac{dN(\xi, z\,|\,\boldsymbol{p})}{d\xi dz}|_{\xi_i, z_i}$. The second term in Equation (12) represents the total number of clusters in the survey, which are selected in ξ and z (and without any selection based on the follow-up observables). Therefore, this term reduces to $\int d\xi dz \Theta_s dN(\xi, z|\boldsymbol{p})/d\xi dz$. With these modifications, and after explicitly setting the survey selection, the likelihood function becomes

$$
\begin{aligned}
\ln \mathcal{L}(\boldsymbol{p}) = \sum_i \ln \frac{dN(\xi, z|\boldsymbol{p})}{d\xi dz}|_{\xi_i, z_i} \\
- \int_{z_{cut}}^{\infty} dz \int_{\xi_{cut}}^{\infty} d\xi \frac{dN(\xi, z|\boldsymbol{p})}{d\xi dz} \\
+ \sum_j \ln P(Y_X, g_t|\xi_j, z_j, \boldsymbol{p})|_{Y_{X_j}, g_{t_j}}
\end{aligned}
\tag{13}
$$

up to a constant. The first sum runs over all clusters i in the sample, and the second sum runs over all clusters j with Y_X and/or WL g_t measurements.

The first two terms in Equation (13) can be interpreted as the likelihood of the abundance (or number counts) of SZ clusters, while the third term represents the information from follow-up mass calibration. These two components are also visualized in the analysis flowchart in Figure 3: the number counts on the lower left side use the distribution of clusters in (ξ, z) space, and the mass calibration on the lower right also uses all available WL and X-ray follow-up data.

We note that the subsamples of clusters that were targeted for follow-up WL and/or X-ray data were selected at random within some cuts in ξ and redshift. Importantly, the selection was not made on WL and/or X-ray measurements. Therefore, the likelihood function presented above is complete; importantly, it does not suffer from biases from WL and/or X-ray selections.

Table 1
WL Modeling Parameters (S18; D19)

Effect	Parameter	Impact on Mass	
		Megacam	*HST*
Intrinsic scatter	$\sigma_{\text{intrinsic}}$	0.214	0.26–0.42
Δ(Intrinsic scatter)	$\Delta\sigma_{\text{intrinsic}}$	0.04	0.021–0.055
Uncorrelated LSS scatter	σ_{LSS}	$9 \times 10^{13}\, M_\odot$	$8 \times 10^{13}\, M_\odot$
Δ(Uncorrelated LSS scatter)	$\Delta\sigma_{\text{LSS}}$	$10^{13}\, M_\odot$	$10^{13}\, M_\odot$
WL mass bias	$b_{\text{WL mass}}$	0.938	0.81–0.92
Mass modeling uncertainty	$\Delta b_{\text{WL mass model}}$	4.4%	5.8%–6.1%
Systematic measurement uncertainty	$\Delta b_{\text{measurement systematics}}$	3.5%	7.2%
Total systematic uncertainty	N/A	5.6%	9.2%–9.4%

Note. The WL mass bias and the (lognormal) intrinsic scatter are calibrated against N-body simulations. Among other effects, they also account for the uncertainty and the scatter in the $c(M)$ relation. This is done separately for each cluster in the *HST* sample leading to a range of values; here we report the smallest and largest individual values. The mass modeling uncertainty accounts for uncertainties in the calibration against N-body simulations and in the centering distribution. The systematic measurement uncertainties account for a multiplicative shear bias and the uncertainty in estimating the redshift distribution of source galaxies. Uncorrelated large-scale structure along the line of sight leads to an additional, Gaussian scatter.

3.2.1. Implementation of the Likelihood Function

We compute the individual terms in Equation (13) as follows:

$$\frac{dN(\xi, z|\boldsymbol{p})}{d\xi dz} = \iint dM\, d\zeta\, [P(\xi|\zeta)P(\zeta|M, z, \boldsymbol{p}) \\ \times \frac{dN(M, z|\boldsymbol{p})}{dMdz}\Omega(z, \boldsymbol{p})], \quad (14)$$

where $\Omega(z, \boldsymbol{p})$ is the survey volume and $dN(M, z|\boldsymbol{p})/dMdz$ is the HMF. We evaluate Equation (14) in the space (ξ, z) by convolving the HMF with the intrinsic scatter in $P(\zeta|M, z, \boldsymbol{p})$ and the measurement uncertainty in $P(\xi|\zeta)$.

The first term in Equation (13) is computed by evaluating Equation (14) at each cluster's measured (ξ_i, z_i), marginalizing over photometric redshift errors where present. The second term is a simple two-dimensional integral over Equation (14).

Our cluster sample contains 22 SZ detections for which no optical counterparts were found; these were assigned lower redshift limits z_{lim} in Bleem et al. (2015). We used simulations to determine the expected false-detection rate $dN_{\text{false}}(\xi)/d\xi$ given survey specifics (see Section 2.2 and Table 1 in dH16). For each unconfirmed cluster candidate, we evaluate a modified version of the first term in Equation (13),

$$\frac{dN_{\text{unconf. cand.}}(\xi, z|\boldsymbol{p})}{d\xi dz} = \frac{dN_{\text{cluster}}(\xi, z|\boldsymbol{p})}{d\xi dz} \\ + \frac{dN_{\text{false}}(\xi)}{d\xi}, \quad (15)$$

and marginalize over the candidate's allowed redshift range $z_{\text{lim}} < z < \infty$. Note that the total expected number of false detections $\int d\xi dN_{\text{false}}(\xi)/d\xi$ is independent of $\boldsymbol{p}$ and is therefore neglected in Equation (13). The expected number of false detections in the SPT-SZ survey is 18 ± 4, which is consistent with our 22 unconfirmed candidates (dH16). In practice, we obtain essentially unchanged results if we simply discard the 22 optically unconfirmed SZ detections from the catalog. There are nine clusters that are detected in the overlap region between adjacent SPT fields. We follow dH16 and double-count these clusters in our analysis. Accounting for

only one object of each pair of these clusters instead does not change our results in any significant way.

The mass calibration term in Equation (13) is computed as

$$P(Y_X^{\text{obs}}, g_t^{\text{obs}}|\xi, z, \boldsymbol{p}) \\ = \int\int\int\int dM\, d\zeta\, dY_X dM_{\text{WL}} \\ \times [P(Y_X^{\text{obs}}|Y_X)P(g_t^{\text{obs}}|M_{\text{WL}})P(\xi|\zeta) \\ \times P(\zeta, Y_X, M_{\text{WL}}|M, z, \boldsymbol{p})P(M|z, \boldsymbol{p})], \quad (16)$$

with the HMF $P(M|z, \boldsymbol{p})$ and the multi-observable scaling relation $P(\zeta, Y_X, M_{\text{WL}}|M, z, \boldsymbol{p})$ that includes the effects of correlated scatter. Computing this multidimensional integral in the $(\zeta, Y_X, M_{\text{WL}})$ space is expensive. We minimize the computational cost of this step by (i) only considering parts of the $(\zeta, Y_X, M_{\text{WL}})$ space that have non-negligible probability densities (we estimate this subspace from the measurements and $\boldsymbol{p}$), (ii) using fast Fourier transform convolutions, and (iii) only performing this computation for clusters that actually have both follow-up measurements Y_X and M_{WL}; otherwise, we restrict the computation to the much cheaper two-dimensional (Y_X, ζ) or (M_{WL}, ζ) spaces. The mass calibration term does not need to be computed at all for clusters that have no X-ray or WL follow-up data.

3.2.2. Update of the X-Ray Analysis Scheme

The X-ray observable is a measurement of the radial Y_X profile. The scaling relation, on the other hand, predicts a value of the observable integrated out to r_{500} for a given M_{500}. In a self-consistent analysis, the likelihood should be extracted by comparing the data and the model prediction at the same radius.

In previous SPT analyses, a Y_X value was extracted from the profile by iteratively solving for the radius r_{iter} at which the measured Y_X and the X-ray scaling relation prediction from Equation (2) match (the scaling relation is evaluated at $M_{500} \equiv 4\pi/3 r_{\text{iter}}^3 500\rho_c$). This iteration was repeated for each set of parameters $\boldsymbol{p}$, but within a fixed reference cosmology. However, this method introduces a bias, because r_{iter} is not equal to the radius r_{500} at which the scaling relation $P(\zeta, Y_X, M_{\text{WL}}|M_{500}, z, \boldsymbol{p})$ in Equation (16) is evaluated.

We choose a different approach and evaluate both the (integrated) measured profile and the model prediction at a fixed fiducial radius $r_{\rm fid}$. We define $r_{\rm fid}$ for each cluster by computing $r_{\rm 500,fid}$ from its SZ significance ξ using a fiducial set of SZ scaling relation parameters and setting $r_{\rm fid} = r_{\rm 500,fid}$. Then, for each set of parameters $\boldsymbol{p}$ in the analysis, we convert the model prediction $Y_{\rm X}(r_{500})$ from radius r_{500} to $r_{\rm fid}$. We use the fact that the radial profiles are well approximated by power laws in radius

$$\frac{Y_{\rm X}(r)}{Y_{\rm X}(r_{500})} = \left(\frac{r}{r_{500}}\right)^{d \ln Y_{\rm X}/d \ln r}, \qquad (17)$$

where r_{500} is derived from M_{500c}. In our analysis, we assume isothermality (see Section 2.2), and so $d \ln Y_{\rm X}/d \ln r$ equals the radial slope in gas mass $d \ln M_{\rm g}/d \ln r$. From our sample we measure

$$d \ln M_{\rm g}/d \ln r = 1.12 \pm 0.23. \qquad (18)$$

We are now able to make a model prediction at $r_{\rm fid}$, starting from the scaling relation prediction $Y_{\rm X}(r_{500})$:

$$Y_{\rm X}(r_{\rm fid}) = Y_{\rm X}(r_{500}) \left(\frac{r_{\rm fid}}{r_{500}}\right)^{d \ln M_{\rm g}/d \ln r}. \qquad (19)$$

In the analysis, we marginalize over the uncertainty in $d \ln M_{\rm g}/d \ln r$, which shows negligible correlation with any other parameter. Note that this prescription for the model prediction $Y_{\rm X}$ $(r_{\rm fid})$ contains an additional dependence on r_{500} and thus on M_{500}.

We note that a similar approach was adopted by other groups (e.g., Mantz et al. 2010a, 2015). We have shown through tests against mock catalogs that the new analysis scheme is unbiased and that the previous method biased $B_{Y_{\rm X}}$ low at a level that is comparable to the uncertainty on that parameter, while the effect on other parameters was very small.

3.3. The Halo Mass Function

We assume the HMF fit by Tinker et al. (2008). This approach assumes universality of the HMF across the cosmological parameter space considered in this work and uses a fitting function that was calibrated against N-body simulations. In principle, the HMF is also affected by baryonic effects. However, hydrodynamic simulations suggest that these have negligible impact for clusters with masses as high as those considered here (Velliscig et al. 2014); this was explicitly tested for a simulated and idealized SPT-SZ cluster survey (Bocquet et al. 2016). Finally, note that the Tinker et al. (2008) fit applies to mean spherical overdensities in the range $200 \leqslant \Delta_{\rm mean} \leqslant 3200$, and we thus convert to $\Delta_{500{\rm crit}}$ using $\Delta_{\rm mean}(z) = 500/\Omega_{\rm m}(z)$. As the HMF fit is only calibrated up to $\Delta_{\rm mean} = 3200$, we require $\Omega_{\rm m}(z) \geqslant 500/3200 = 0.15625$ for all redshifts $z \geqslant 0.25$ relevant for our cluster sample.

3.4. Pipeline Validation on Mock Data

We have run extensive tests to ensure that our analysis pipeline is unbiased at a level that is much smaller than our total error budget. The primary approach is testing against mock catalogs. Of course, such tests are only useful if producing mocks is easier and more reliable than the actual analysis. In our case, the analysis is challenging mainly because of the computation of multidimensional integrals. To create one of our mocks, on the other hand, one has to compute the HMF, apply the observable–mass relations, draw random deviates, and compute WL shear profiles. Using the same code to compute the HMF for the mocks and the analysis would undercut the usefulness of the testing, and so we also created mocks using HMFs computed with an independent code. For the same reason, the mock shear profiles were created using an independent code. We typically create mock catalogs that contain an order of magnitude more clusters and calibration data than our real sample. We created and analyzed sets of mocks using different random seeds and different sets of input parameters (notably, some with $w \neq -1$). No test indicated any biases in our analysis pipeline at the level relevant for our data set.

3.5. Quantifying Posterior Distribution (Dis)agreement

We characterize the agreement between constraints obtained from pairs of probes (e.g., clusters and primary CMB anisotropies) by quantifying whether the difference between the two posterior distributions is consistent with zero difference. We draw representative samples $[\boldsymbol{x}_1]$ and $[\boldsymbol{x}_2]$ from the posteriors of the two probes $P_1(\boldsymbol{x})$ and $P_2(\boldsymbol{x})$, compute the difference between all pairs of points $\boldsymbol{\delta} \equiv \boldsymbol{x}_1 - \boldsymbol{x}_2$, and then construct the probability distribution D from the ensemble $[\boldsymbol{\delta}]$. The probability value (or p-value) that the two distributions represent the same underlying quantity is

$$p = \int_{D < D(0)} d\delta D(\boldsymbol{\delta}), \qquad (20)$$

where $D(0)$ is the probability of zero difference. The p-value can be converted into a significance assuming Gaussian statistics. This measure can be applied to one-dimensional and multi-dimensional parameter spaces. The code is publicly available.[54]

3.6. Parameter Priors and Likelihood Sampling

In our cosmological fits, we assume spatial flatness and allow the sum of neutrino masses to vary. The comparison of our results with constraints from primary CMB anisotropies is of prime interest—notably, the comparison of constraints on σ_8. For primary CMB anisotropies, σ_8 is strongly degenerate with $\sum m_\nu$, and so the latter should be a free parameter of the model to avoid artificially tight constraints. We refer to the flat ΛCDM model with a varying sum of neutrino masses as $\nu\Lambda$CDM and to its extension with a free dark energy equation-of-state parameter as νwCDM.

In the $\nu\Lambda$CDM cosmology, we vary the cosmological parameters $\Omega_{\rm m}$, $\Omega_\nu h^2$, $\Omega_{\rm b} h^2$, A_s, h, n_s; σ_8 is a derived parameter. Our cluster data primarily constrain $\Omega_{\rm m}$ and σ_8, and we marginalize over flat priors on the other parameters. The parameter ranges for $\Omega_{\rm b} h^2$ and n_s are chosen to roughly match the 5σ credibility interval of the *Planck* constraints; h is allowed to vary in the range 0.55–0.9. We assume two massless neutrinos and one massive neutrino and allow $\Omega_\nu h^2$ to vary in the range 0–0.01; this corresponds to a range in $\sum m_\nu$ of 0–0.93 eV. We note that the minimum allowed sum of neutrino masses from oscillation experiments is $\sum m_\nu > 59.5 \pm 0.5$ meV (Tanabashi et al. 2018). In a departure from previous SPT analyses, we do not apply a BBN prior on $\Omega_{\rm b} h^2$ or constraints from direct measurements of H_0. We remind the reader that the implementation of the theory HMF leads to an effective, hard prior $\Omega_{\rm m}(z) \gtrsim 0.16$ for all redshifts $z > 0.25$ relevant to our survey (see Section 3.3); however, this prior does not affect our results. All parameters and their priors are summarized in Table 2.

---

[54] https://github.com/SebastianBocquet/PosteriorAgreement

The likelihood sampling is done within COSMOSIS using the METROPOLIS (Metropolis et al. 1953) and MULTINEST (Feroz et al. 2009) samplers. We confirmed that they produce consistent results.

4. Results

Our fiducial results are obtained from the SPT-selected clusters with their detection significances and redshifts, together with the WL and X-ray follow-up data where available. We refer to this data set as SPTcl (SPT-SZ $+$WL$+Y_X$).

Constraints on cosmological and scaling relation parameters are summarized in Table 3. We also provide constraints on the parameter combination $\sigma_8(\Omega_m/0.3)^{0.2}$ and $\sigma_8(\Omega_m/0.3)^{0.5}$; the exponent $\alpha = 0.2$ is chosen, as it minimizes the fractional uncertainty on $\sigma_8(\Omega_m/0.3)^\alpha$, and $\alpha = 0.5$ is common in other low-redshift cosmological probes.

4.1. $\nu\Lambda CDM$ Cosmology

From the cluster abundance measurement of our SPTcl (SPT-SZ $+$WL$+Y_X$) data set we obtain our baseline results

$$\Omega_m = 0.276 \pm 0.047 \tag{21}$$

$$\sigma_8 = 0.781 \pm 0.037 \tag{22}$$

$$\sigma_8(\Omega_m/0.3)^{0.2} = 0.766 \pm 0.025. \tag{23}$$

The remaining cosmological parameters (including $\sum m_\nu$; see Figure 9) are not or only weakly constrained by the cluster data. Constraints on scaling relation parameters can be found in Table 3. We note that applying priors on $\Omega_b h^2$ and H_0 from BBN and direct measurements of H_0 and/or fixing the sum of neutrino masses to 0.06 eV, approximately the lower limit predicted from terrestrial oscillation experiments, does not affect our constraints on Ω_m and σ_8 in any significant way (see Figure 15 in Appendix A for the impact of fixing the sum of the neutrino masses).

4.1.1. Goodness of Fit

In Figure 4, we compare the measured distribution of clusters as a function of their redshift and SPT detection significance with the model prediction evaluated for the recovered parameter constraints. This figure does not suggest any problematic feature in the data.

For a more quantitative discussion, we bin our confirmed clusters into a grid of 30×30 in redshift and detection significance, and we confront this measurement with the expected number of objects in each two-dimensional bin. The expected (and measured) numbers in each bin are too small to apply Gaussian χ^2 statistics, and we estimate the goodness of fit using a prescription for the Poisson statistic (Kaastra 2017).[55] This approach is similar to our likelihood analysis, which applies Poisson statistics within infinitesimally small bins, instead of the larger bins we assume here. Adopting the maximum-posterior $\nu\Lambda CDM$ parameters, we compute the expected number of clusters in each of the 30×30 bins and follow Kaastra (2017) to evaluate the test statistic C. We obtain an expected mean C_e and variance C_v,

$$C_e = 439.8; \quad C_v = 26.8^2. \tag{24}$$

---

[55] We use the PYTHON implementation from https://github.com/abmantz/cstat.

Parameter	Prior
Cosmological	
Ω_m	$\mathcal{U}(0.05, 0.6)$, $\Omega_m(z > 0.25) > 0.156$
$\Omega_b h^2$	$\mathcal{U}(0.020, 0.024)$
$\Omega_\nu h^2$	$\mathcal{U}(0, 0.01)$
Ω_k	Fixed (0)
A_s	$\mathcal{U}(10^{-10}, 10^{-8})$
h	$\mathcal{U}(0.55, 0.9)$
n_s	$\mathcal{U}(0.94, 1.00)$
w	Fixed (-1) or $\mathcal{U}(-2.5, -0.33)$
Optical Depth to Reionization	
τ	Fixed or $\mathcal{U}(0.02, 0.14)$
SZ Scaling Relation	
A_{SZ}	$\mathcal{U}(1, 10)$
B_{SZ}	$\mathcal{U}(1, 2.5)$
C_{SZ}	$\mathcal{U}(-1, 2)$
$\sigma_{\ln\zeta}$	$\mathcal{U}(0.01, 0.5)$ $(\times\mathcal{N}(0.13, 0.13^2))$
X-ray Y_X Scaling Relation	
A_{Y_X}	$\mathcal{U}(3, 10)$
B_{Y_X}	$\mathcal{U}(0.3, 0.9)$
C_{Y_X}	$\mathcal{U}(-1, 0.5)$
$\sigma_{\ln Y_X}$	$\mathcal{U}(0.01, 0.5)$
$d \ln M_g/d \ln r$	$\mathcal{U}(0.4, 1.8) \times \mathcal{N}(1.12, 0.23^2)$
WL Modeling	
$\delta_{WL,bias}$	$\mathcal{U}(-3, 3) \times \mathcal{N}(0, 1)$
$\delta_{Megacam}$	$\mathcal{U}(-3, 3) \times \mathcal{N}(0, 1)$
δ_{HST}	$\mathcal{U}(-3, 3) \times \mathcal{N}(0, 1)$
$\delta_{WL,scatter}$	$\mathcal{U}(-3, 3) \times \mathcal{N}(0, 1)$
$\delta_{WL,LSS_{Megacam}}$	$\mathcal{U}(-3, 3) \times \mathcal{N}(0, 1)$
$\delta_{WL,LSS_{HST}}$	$\mathcal{U}(-3, 3) \times \mathcal{N}(0, 1)$
Correlated Scatter	
ρ_{SZ-WL}	$\mathcal{U}(-1, 1)$
ρ_{SZ-X}	$\mathcal{U}(-1, 1)$
ρ_{X-WL}	$\mathcal{U}(-1, 1)$
	$\det(\Sigma_{multi-obs}) > 0$

Note. The Gaussian prior on $\sigma_{\ln\zeta}$ is only applied when no X-ray data are included in the fit. The parameter ranges for $\Omega_b h^2$ and n_s are chosen to roughly match the 5σ interval of the *Planck* ΛCDM results. w is fixed to -1 for ΛCDM and is allowed to vary for wCDM. The optical depth to reionization τ is only relevant when *Planck* data are included in the analysis. The WL modeling systematics are presented in Table 1.

For samples that contain at least a few hundred objects—like ours—the statistic C is well approximated by a Gaussian with mean C_e and variance C_v (Kaastra 2017). The data statistic for our sample is

$$C_d = 449.3, \tag{25}$$

in full agreement with the range expected for C_e, indicating that the model provides an adequate fit to the data.

4.1.2. Comparison with Previous SPT Results

As discussed in the Introduction, this work uses the same SPT-SZ cluster sample (Bleem et al. 2015, now with updated photometric redshifts; see Section 2.1) that was analyzed

Table 3
Constraints on a Subset of Cosmological and Scaling Relation Parameters

Parameter	$\nu\Lambda$CDM			νwCDM		
	SPT-SZ+WL	SPTcl	*Planck*+SPTcl	SPTcl	*Planck*+SPTcl	*Planck*+BAO+SNIa+SPTcl
Ω_{m}	0.285 ± 0.047	0.276 ± 0.047	0.353 ± 0.027	0.299 ± 0.049	0.347 ± 0.039	0.305 ± 0.008
σ_8	0.763 ± 0.037	0.781 ± 0.037	0.761 ± 0.033	0.766 ± 0.036	0.761 ± 0.027	0.801 ± 0.026
$\sigma_8(\Omega_{\mathrm{m}}/0.3)^{0.2}$	0.753 ± 0.025	0.766 ± 0.025	0.786 ± 0.025	0.763 ± 0.024	0.782 ± 0.018	0.803 ± 0.024
$\sigma_8(\Omega_{\mathrm{m}}/0.3)^{0.5}$	0.739 ± 0.041	0.745 ± 0.042	0.824 ± 0.020	0.760 ± 0.043	0.816 ± 0.032	0.807 ± 0.023
h	...	...	0.645 ± 0.019	...	0.657 ± 0.039	0.681 ± 0.009
$\sum m_\nu$ (eV)	...	...	0.39 ± 0.19	...	0.50 ± 0.24	0.16 ± 0.10
w	-1	-1	-1	-1.55 ± 0.41	-1.12 ± 0.21	-1.03 ± 0.04
A_{SZ}	$5.68^{+0.89}_{-1.03}$	$5.24^{+0.76}_{-0.93}$	$4.58^{+0.63}_{-0.92}$	$4.84^{+0.80}_{-0.97}$	$4.57^{+0.55}_{-0.62}$	$4.07^{+0.62}_{-0.76}$
B_{SZ}	$1.519^{+0.087}_{-0.110}$	$1.534^{+0.099}_{-0.100}$	$1.667^{+0.069}_{-0.072}$	$1.601^{+0.098}_{-0.102}$	$1.653^{+0.079}_{-0.081}$	$1.685^{+0.074}_{-0.088}$
C_{SZ}	$0.547^{+0.468}_{-0.375}$	$0.465^{+0.492}_{-0.321}$	$0.993^{+0.222}_{-0.218}$	$1.290^{+0.443}_{-0.250}$	$1.117^{+0.221}_{-0.191}$	$0.746^{+0.165}_{-0.169}$
$\sigma_{\ln\zeta}$	$0.152^{+0.066}_{-0.099}$	$0.161^{+0.084}_{-0.075}$	$0.162^{+0.083}_{-0.100}$	$0.169^{+0.082}_{-0.072}$	$0.148^{+0.073}_{-0.106}$	$0.133^{+0.055}_{-0.133}$
$A_{Y_{\mathrm{X}}}$	...	$6.35^{+0.68}_{-0.69}$	$7.55^{+0.57}_{-0.56}$	$6.33^{+0.69}_{-0.78}$	$7.44^{+0.60}_{-0.68}$	$7.38^{+0.63}_{-0.65}$
$B_{Y_{\mathrm{X}}}$	...	$0.514^{+0.032}_{-0.042}$	$0.480^{+0.028}_{-0.035}$	$0.499^{+0.032}_{-0.039}$	$0.488^{+0.032}_{-0.037}$	$0.480^{+0.033}_{-0.041}$
$C_{Y_{\mathrm{X}}}$	...	$-0.310^{+0.140}_{-0.209}$	$-0.464^{+0.131}_{-0.133}$	$-0.669^{+0.120}_{-0.213}$	$-0.525^{+0.141}_{-0.143}$	$-0.371^{+0.123}_{-0.120}$
$\sigma_{\ln Y_{\mathrm{X}}}$	...	$0.184^{+0.087}_{-0.089}$	$0.180^{+0.095}_{-0.102}$	$0.170^{+0.076}_{-0.094}$	$0.205^{+0.094}_{-0.087}$	$0.181^{+0.102}_{-0.162}$

Note. SPTcl stands for the SPT-SZ+WL+Y_{X} data set, and *Planck* refers to the TT+lowTEB data. The cluster-based posterior distributions for h and $\sum m_\nu$ are poorly constrained and strongly affected by the hard priors applied, and we therefore do not quote constraints.

in dH16, and the key update is the inclusion of WL data. In dH16, the amplitude of the observable–mass relation was set by a prior on the X-ray normalization $A_{Y_{\mathrm{X}}}$, which in turn was informed by external WL data sets (CCCP and WtG; Applegate et al. 2014; von der Linden et al. 2014; Hoekstra et al. 2015). Gaussian priors were applied to the remaining SZ and X-ray scaling relation parameters, which we dropped for this analysis. In Figure 5, we compare our constraints on Ω_{m}–σ_8 with the ones presented in dH16. We recover very similar results; in Ω_{m}–σ_8 space, the agreement is $p = 0.86$ (0.2σ). Since the key difference between dH16 and this work is the inclusion of WL data, this agreement indirectly confirms that our internal WL mass calibration agrees with the external priors adopted previously. This is expected because the X-ray prior adopted in previous work agrees well with the measurement enabled by our own WL data set (D19).

4.1.3. Comparison with External Probes

In Figure 6, we show a comparison of our results with constraints from *Planck* (TT+lowTEB) and from combined analyses of cosmic shear, galaxy–galaxy lensing, and galaxy clustering from the Kilo Degree Survey and the Galaxies And Mass Assembly survey (KiDS+GAMA; van Uitert et al. 2018) and the Dark Energy Survey (DES) Year 1 results (Abbott et al. 2018). We also compare our results with another cluster study that used internal WL mass calibration but a sample based on X-ray selection (Weighing the Giants, or WtG; Mantz et al. 2015). Overall, the constraining power of all probes is roughly similar in this plane. There is good agreement among all probes, as the 68% contours all overlap. In particular, the cluster-based constraints yield very similar Ω_{m}, but WtG favors a somewhat higher σ_8. Interestingly, the degeneracy axis of WtG is slightly tilted with respect to SPTcl, which we attribute to the different redshift and mass ranges spanned by the two samples.

We pay particular attention to a comparison with *Planck* (TT+lowTEB). Our constraint on $\sigma_8(\Omega_{\mathrm{m}}/0.3)^{0.2} = 0.766 \pm 0.025$ is lower than the one from *Planck* ($\sigma_8(\Omega_{\mathrm{m}}/0.3)^{0.2} = 0.814^{+0.041}_{-0.020}$); the agreement between the two measurements is $p = 0.28$ (1.1σ). In the two-dimensional Ω_{m}–σ_8 space, the agreement is $p = 0.13$ (1.5σ).

We note that the latest analysis of the cluster sample selected by the *Planck* satellite is qualitatively in agreement with our constraint, as shown in Figure 32 of Planck Collaboration et al. (2018b). Notably, the 95% contour of their result, calibrated using CMB lensing, encompasses the *Planck* primary CMB result in the Ω_{m}–σ_8 plane.

4.1.4. Impact of X-Ray Follow-up Data

We compare our baseline results from SPTcl (SPT-SZ+WL +Y_{X}) with the ones obtained from the SPT-SZ+WL data combination, in which no X-ray follow-up data are included. In this case, we apply an informative Gaussian prior to the SZ scatter $\sigma_{\ln\zeta}$. As in all of this work, no informative priors are applied on the remaining three SZ scaling relation parameters and on the X-ray scaling relation parameters. A figure showing constraints on all relevant parameters can be found in Appendix B (Figure 16, compare blue and red contours), and Table 3 summarizes parameter constraints. Both data combinations, with and without X-ray data, provide very similar constraints on cosmological and scaling relation parameters. Without informative priors on the X-ray amplitude, mass slope, or redshift evolution, the inclusion of X-ray data does not enable tighter constraints. The use of X-ray data does, however, enable constraints on the SZ and X-ray scatters $\sigma_{\ln\zeta}$ and $\sigma_{\ln Y_{\mathrm{X}}}$, with flat priors applied to both.

Note that our data set is sensitive to the SZ-to-X-ray relation. As defined in Section 3.1, our model consists of two observable–mass relations that each relate one observable to mass. This implies that the amplitudes, mass slopes, and redshift evolutions of the two scaling relations are degenerate, as shown in Figure 7. The degeneracy between $\sigma_{\ln\zeta}$ and $\sigma_{\ln Y_{\mathrm{X}}}$ is particularly interesting: while the marginalized posterior of either or both parameters has substantial mass near 0 scatter (see Figure 16), the bottom right panel of Figure 7 shows that 0 total scatter is clearly ruled out.

Our data set is not able to constrain any of the coefficients describing the correlated scatter among the observables. The visual impression of a constraint in Figure 16 stems from the requirement that the matrix describing the multi-observable
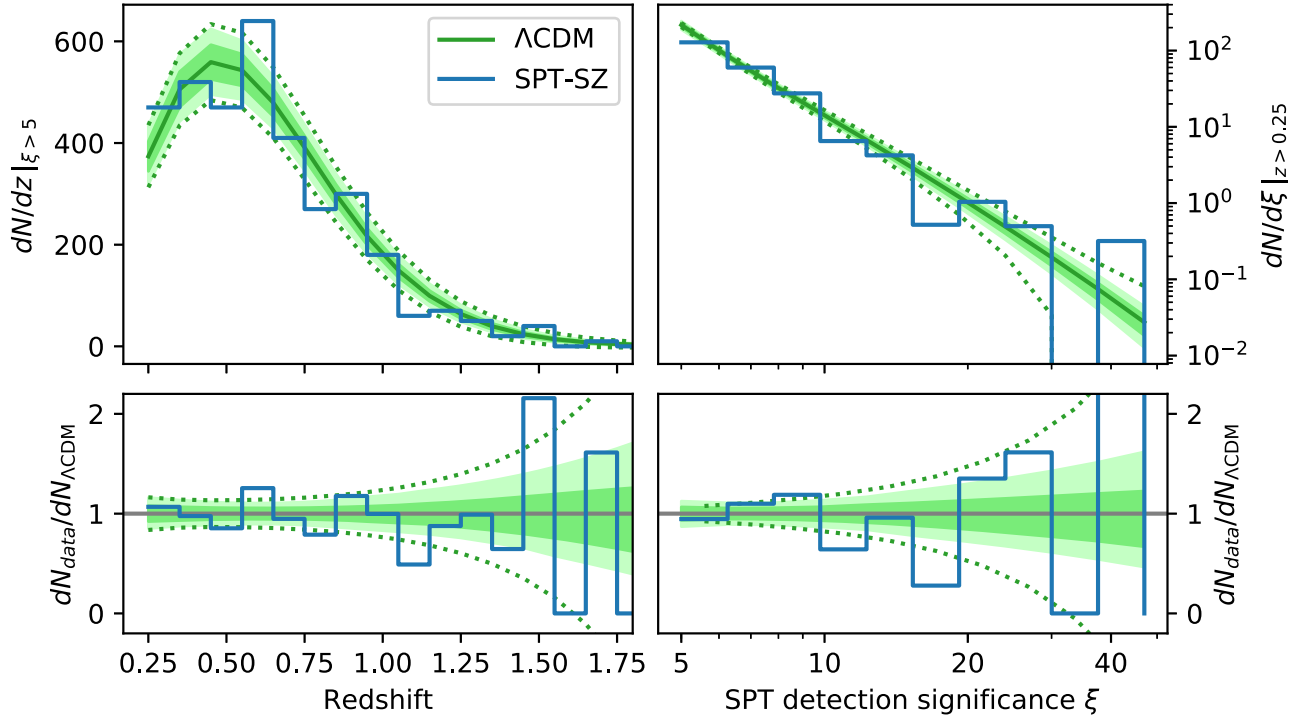
Figure 4. Distribution of clusters as a function of redshift (left panels) and detection significance ξ (right panels). The top panels show the SPT-SZ data and the recovered model predictions for $\nu\Lambda$CDM. The bottom panels show the residuals of the data with respect to the model prediction. The different lines and shadings correspond to the mean recovered model and the 1σ and 2σ allowed ranges. The dotted lines show the Poisson error on the mean model prediction. There are no clear outliers, and we conclude that the model provides an adequate fit to the data.
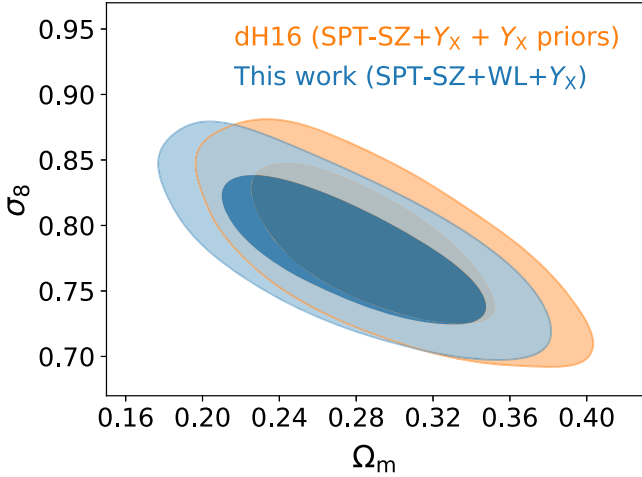
Figure 5. Constraints on Ω_m and σ_8 from this analysis and from a previous analysis that used the same cluster sample (dH16). The consistency (0.2σ) indicates that our internal mass calibration using WL data agrees with the external X-ray mass calibration priors adopted in dH16.

Figure 6. $\nu\Lambda$CDM constraints on Ω_m and σ_8. The SPTcl data set comprises SPT-SZ+WL+Y_X, *Planck* is TT+lowTEB, and KiDS+GAMA and DES Y1 are cosmic shear+galaxy clustering+galaxy–galaxy lensing. The WtG (X-ray-selected clusters) result also contains their f_{gas} measurement.

scatter must be a valid non-degenerate covariance matrix that prevents combinations of extreme correlation coefficients.

4.1.5. Constraints on X-Ray Scaling Relation Parameters

Without any informative priors on the X-ray scaling relation parameters, we can use the SPTcl data set to constrain the Y_X–mass relation. The recovered amplitude

$$A_{Y_X} = 6.35 \pm 0.69 \tag{26}$$

is very close to the WL-informed prior (Applegate et al. 2014; von der Linden et al. 2014; Hoekstra et al. 2015; Mantz et al. 2015)

that was used in our previous cosmology analysis ($A_{Y_X} = 6.38 \pm 0.61$; dH16). We constrain the redshift evolution of the Y_X–mass relation to

$$C_{Y_X} = -0.31^{+0.14}_{-0.21}. \tag{27}$$

The self-similar expectation $C_{Y_X} = -0.4$ is well within 1σ. Our measurement of the Y_X scatter

$$\sigma_{\ln Y_X} = 0.18 \pm 0.09 \tag{28}$$

is higher than but consistent at the 1σ level with the prior 0.12 ± 0.08 adopted in previous SPT analyses. It closely
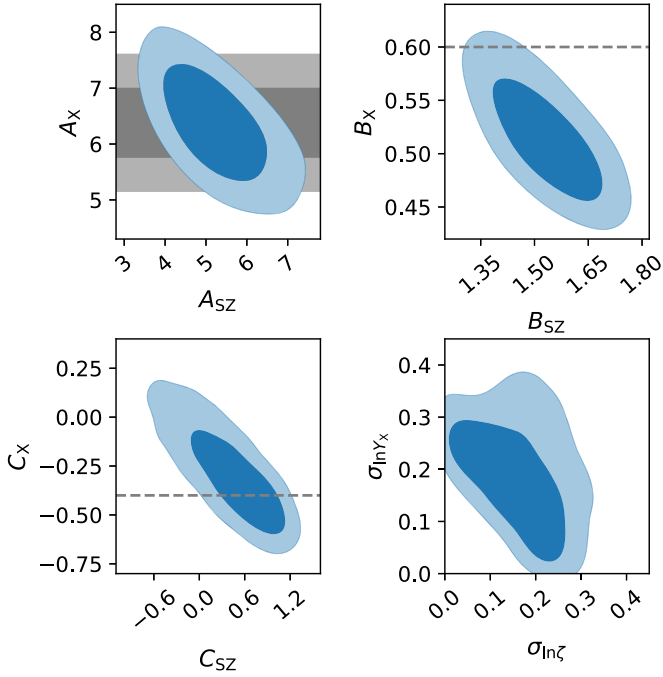
Figure 7. Our data set is sensitive to the joint SZ–X-ray relation, which leads to correlations between the SZ and X-ray scaling relation amplitudes A (top left), mass slopes B (top right), redshift evolutions C (bottom left), and intrinsic scatters σ (bottom right). We also show the external WL-informed prior on the X-ray amplitude A_{Y_X} applied in dH16, as well as the self-similar expectations for the X-ray slope B_{Y_X} and redshift evolution C_{Y_X}.

matches the measurement 0.182 ± 0.015 from Mantz et al. (2016), although with larger uncertainty.

The recovered Y_X mass slope

$$B_{Y_X} = 0.514 \pm 0.037 \qquad (29)$$

is lower than the self-similar evolution $B_{Y_X} = 0.6$ and the measurements $B_{Y_X} = 0.57 \pm 0.03$ from Vikhlinin et al. (2009a) and $B_{Y_X} = 1/(1.61 \pm 0.04) = 0.621 \pm 0.015$ from Mantz et al. (2016).[56] From our data, the consistency of B_{Y_X} with the self-similar value is $p = 0.021$, corresponding to 2.3σ. Our data constrain B_{Y_X} through its degeneracy with the SZ mass slope B_{SZ} (Figure 7), which in turn is constrained through the process of fitting the cluster abundance against the HMF. This subject was already discussed in dH16, where a prior on B_{Y_X} was adopted from the measurement by Vikhlinin et al. (2009a).

As a cross-check, and because other groups have used the X-ray gas mass as their low-scatter mass proxy, we repeat the analysis replacing the Y_X data with M_{gas} measurements. We apply no informative priors on the four parameters of the M_{gas} scaling relation of Equation (7). We then analyze this SPT-SZ +WL+M_{gas} data set. The constraints on the SZ scaling relation parameters and cosmology are very similar to the results from the fiducial SPT-SZ+WL+Y_X analysis, and again we observe an X-ray mass slope that disagrees with the self-similar evolution. We measure

$$A_{M_g} = 0.116 \pm 0.011 \qquad (30)$$

$$B_{M_g} = 1.22 \pm 0.07 \qquad (31)$$

$$C_{M_g} = -0.05 \pm 0.17 \qquad (32)$$

$$\sigma_{\ln M_g} = 0.11 \pm 0.04. \qquad (33)$$

This corresponds to a 2.5σ preference for a slope that is steeper than the self-similar expectation $B_{M_g} = 1$ or the measurement $B_{M_g} = 1.004 \pm 0.014$ from Mantz et al. (2016). The measurement $B_{M_g} = 1.15 \pm 0.02$[57] from Vikhlinin et al. (2009a) is in between the two results and is 1σ low compared to ours. Because these slopes differ, we compare the measurements of the gas fraction A_{M_g} at the pivot mass in our relation $5 \times 10^{14}\, M_\odot/h_{70}$, where we obtain Equation (30). The mean gas fraction at this mass is 0.128 from Mantz et al. (2016) and 0.114 from Vikhlinin et al. (2009a). Both values are contained within the 1σ range of our measurement. Finally, as for Y_X, our measurement of the redshift evolution encompasses the self-similar evolution ($C_{M_g} = 0$) within 1σ.

For an extensive discussion of the mass and redshift trends in the M_{gas}–mass and Y_X–mass relations for SPT-selected clusters and how they compare to previously published results, we refer the reader to two recent studies where SZ-based mass information was adopted using the posterior distributions of the SZ ζ–mass relation parameters presented in dH16 (Chiu et al. 2018; Bulbul et al. 2019). Bulbul et al. (2019) used X-ray data from *XMM-Newton*, while we use data from *Chandra*; their recovered constraints on the X-ray mass slopes and redshift evolutions are consistent with our findings at the 1σ level, which confirms a consistent X-ray analysis. Here we note that most measurements of X-ray scaling relations have been performed using samples at low redshifts $z \lesssim 0.5$, and so it is of particular interest to examine the mass slopes for the low-redshift half of our sample.

We therefore split our cluster sample (and all follow-up data) into two subsamples above and below $z = 0.6$, the median redshift of our sample. Constraints on the most relevant parameters are shown in Figure 16 in Appendix B, and Figure 8 shows the constraints on B_{Y_X}. Interestingly, the low-redshift subsample prefers a higher value

$$B_{Y_X}(0.25 < z < 0.6) = 0.583^{+0.054}_{-0.069} \qquad (34)$$

that is closer to the self-similar evolution $B_{Y_X} = 0.6$. As expected, the value obtained from the high-z subsample,

$$B_{Y_X}(z > 0.6) = 0.503^{+0.037}_{-0.047}, \qquad (35)$$

is lower than the one obtained from the full sample. However, note that the low-redshift and high-redshift constraints on B_{Y_X} only differ with $p = 0.44$ (0.8σ).

We perform the same splits in redshift using the SPT-SZ +WL+M_{gas} data set. Here as well, our measurement using the low-redshift subsample,

$$B_{M_g}(0.25 < z < 0.6) = 1.12 \pm 0.09, \qquad (36)$$

is closer to the self-similar evolution, while the high-redshift half yields a steeper slope

$$B_{M_g}(z > 0.6) = 1.36 \pm 0.11. \qquad (37)$$

To capture a possible redshift dependence of the slope of the X-ray scaling relations, we analyzed models with an extended

---

[56] The scaling relation in Mantz et al. (2016) is defined as a power law in mass, whereas we use a power law in Y_X.

[57] Vikhlinin et al. (2009a) use the functional form $f_{gas} = f_{gas,0} + \alpha \ln M$. The mass dependence α is converted into a power-law exponent in Chiu et al. (2018).
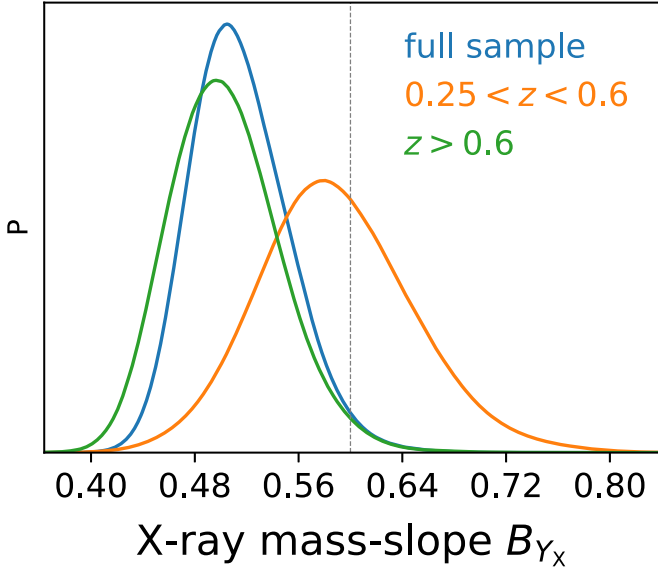
Figure 8. Constraint on the X-ray Y_X slope B_{Y_X} from the full sample, and from the low- and high-z halves. The self-similar expectation $B_{Y_X} = 0.6$ is 2.3σ off the result from the full sample, but within 1σ of the low-z result.

scaling relation model of the form

$$
\begin{aligned}
\ln \mathcal{O}_{\text{X-ray}} = \ln A \; + \; & B \ln \left(\frac{M_{500c} \; h_{70}}{5 \times 10^{14} M_\odot} \right) \\
+ \; & C \ln \left(\frac{E(z)}{E(0.6)} \right) \\
+ \; & E \ln \left(\frac{E(z)}{E(0.6)} \right) \ln \left(\frac{M_{500c} \; h_{70}}{5 \times 10^{14} M_\odot} \right)
\end{aligned}
\tag{38}
$$

that allows for additional freedom and the mass and redshift dependences. However, we do not observe any significant departure in E from 0, in agreement with Bulbul et al. (2019).

4.2. Constraints on the Sum of Neutrino Masses

Having quantified the consistency between our cluster data set and *Planck* in Section 4.1.3, we proceed and combine the two probes. The SPTcl+*Planck* data set yields

$$\Omega_m = 0.353 \; \pm \; 0.027 \tag{39}$$
$$\sigma_8 = 0.761 \; \pm \; 0.033 \tag{40}$$
$$\sigma_8 (\Omega_m / 0.3)^{0.2} = 0.786 \; \pm \; 0.025 \tag{41}$$
$$\sum m_\nu = 0.39 \; \pm \; 0.19 \text{ eV} \tag{42}$$
$$\sum m_\nu \; < 0.74 \text{ eV (95\% upper limit)}. \tag{43}$$

Compared to constraints from *Planck* alone, the combination with SPTcl shrinks the errors on Ω_m, σ_8, and $\sigma_8 (\Omega_m / 0.3)^{0.2}$ by 3%, 12%, and 20%. By breaking parameter degeneracies (notably between σ_8 and $\sum m_\nu$; see Figure 9), the addition of cluster data to the primary CMB measurements by *Planck* affects the inferred sum of neutrino masses. If interpreted as a Gaussian probability distribution (i.e., ignoring the hard cut $\sum m_\nu > 0$), our joint measurement corresponds to a 2.0σ preference for a nonzero sum of neutrino masses.

The Planck Collaboration recently presented an updated analysis of primary CMB anisotropies (Planck Collaboration et al. 2018a). Most notably, the optical depth decreased to $\tau = 0.054 \pm 0.007$.
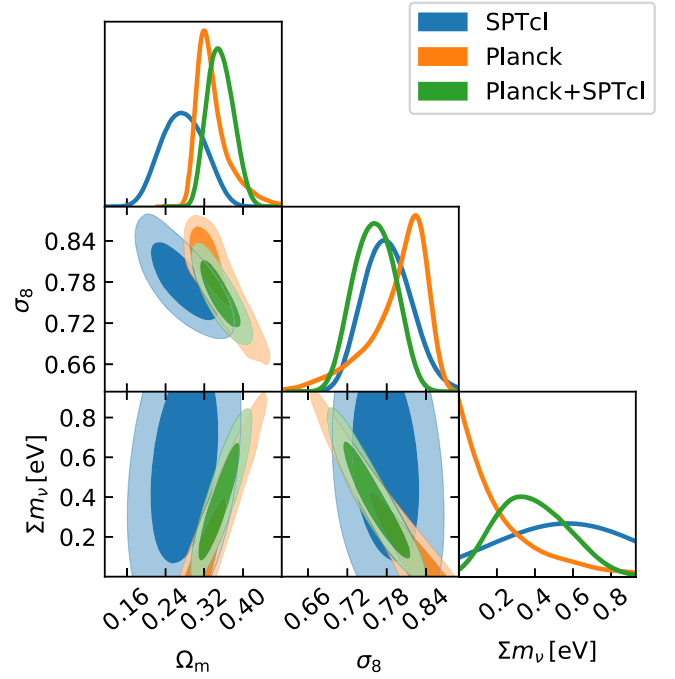
Figure 9. $\nu\Lambda$CDM constraints on Ω_m, σ_8, and $\sum m_\nu$. The SPTcl data set comprises (SPT-SZ+WL+Y_X); *Planck* uses TT+lowTEB. Note that the cluster data constrain Ω_m and σ_8 almost independently of $\sum m_\nu$.

As the updated *Planck* likelihood code is not available yet, we estimate the impact of the updated *Planck* analysis on our results and especially our constraint on $\sum m_\nu$ by analyzing the *Planck* 2015 TT data (without lowTEB) with a prior on $\tau \sim \mathcal{N}(0.054, 0.007^2)$. We analyze the joint SPTcl+*Planck* TT+τ prior data set and obtain

$$\sum m_\nu = 0.35 \; \pm \; 0.21 \text{ eV}. \tag{44}$$

The recovered constraint is lower than our fiducial constraint using the (SPTcl+*Planck* TT+lowTEB) data set, and the 95% credible interval runs against the hard prior $\sum m_\nu = 0$. The preference for a nonzero sum of neutrino masses reduces to 1.7σ. We caution the reader that this result is only preliminary owing to the way it depends on the prior on τ that we adopted. The full analysis will require analyzing our cluster sample jointly with the latest *Planck* analysis.

We explain the shift in $\sum m_\nu$ toward lower values as follows. In ΛCDM, the relationship between A_s and σ_8 is essentially fixed. However, in $\nu\Lambda$CDM, the additional degree of freedom $\sum m_\nu$ allows for different values of σ_8 at a fixed A_s. In any joint analysis of *Planck*+low-redshift growth-of-structure probe such as SPTcl, $\sum m_\nu$ is constrained to accommodate the *Planck* measurement of A_s with the low-redshift measurement of σ_8. As has been pointed out many times, the *Planck*15 measurement of A_s implies a higher σ_8 in ΛCDM than obtained from local measurements, which leads to an apparent detection of $\sum m_\nu$ in $\nu\Lambda$CDM. Meanwhile, CMB temperature fluctuations are sensitive to the combination $A_s e^{-2\tau}$—i.e., A_s and τ are positively correlated in TT parameter constraints—so imposing a τ prior with a lower central value results in a lower inferred value of A_s. In ΛCDM, this shifts the *Planck*-inferred σ_8 to lower values. Finally, when analyzing *Planck* TT+τ+SPTcl in $\nu\Lambda$CDM, σ_8 is dominated by the local constraint from SPTcl, and the lower A_s implies that $\sum m_\nu$ need not be as high as in our fiducial analysis.

We further test the impact of using only the low-redshift half of our cluster sample. The SPTcl($0.25 < z < 0.6$)+*Planck* data set yields

$$\sum m_\nu = 0.29^{+0.09}_{-0.29} \text{ eV.} \tag{45}$$

The probability distribution in $\sum m_\nu$ runs against the hard prior $\sum m_\nu > 0$, which shifts the mean recovered value away from the mode; the 68% credible interval starts at $\sum m_\nu = 0$. In conclusion, all preference for a nonzero sum of neutrino masses vanishes when only considering the low-redshift half of our cluster sample. Figure 10 shows the constraints on $\sum m_\nu$ as obtained in our fiducial analysis, the analysis with the τ prior, and the analysis where we only use the low-redshift cluster data.

The sum of neutrino masses is degenerate with the amplitude of the SZ scaling relation A_{SZ} with a correlation coefficient $\rho_{A_{SZ} - \sum m_\nu} = 0.83$; see Figure 11. Therefore, an improved (WL) mass calibration will improve the constraints on $\sum m_\nu$. Also note that the effect of massive neutrinos on the HMF depends (weakly) on mass and redshift (Ichiki & Takada 2012). Therefore, an improved mass calibration covering the entire cluster sample will in principle allow for measurements of the sum of neutrino masses from clusters alone.

4.3. νwCDM Cosmology

We consider an extension to modeling dark energy as a cosmological constant by allowing for an equation-of-state parameter w that is different from $w = -1$. This modification impacts the expansion history of the universe $E(z)$ and the growth of structure; both affect the cluster abundance. Therefore, as noted in, e.g., Haiman et al. (2001), measuring the abundance over a range of redshifts allows for a measurement of w. Using our SPTcl data set, we obtain

$$w = -1.55 \pm 0.41 \tag{46}$$
$$\Omega_m = 0.299 \pm 0.049 \tag{47}$$
$$\sigma_8 = 0.766 \pm 0.036, \tag{48}$$

as shown by the blue contours in Figure 12. Constraints on scaling relation parameters can be found in Table 3. The consistency of our recovered constraint on w with a cosmological constant $w = -1$ has a p-value 0.076 (1.8σ). Note that the SPTcl contours in the Ω_m–σ_8–w space close.

Our constraint on w is in general agreement with the result obtained from the SPT-SZ+Y_X+X-ray priors data combination $w = -1.28 \pm 0.31$ as presented in dH16. In that earlier analysis, informative (Gaussian) priors were applied on the scaling relation parameters A_{SZ}, B_{SZ}, C_{SZ}, $\sigma_{\ln\zeta}$, A_{Y_X}, B_{Y_X}, C_{Y_X}, $\sigma_{\ln Y_X}$, whereas we marginalize over flat priors and use our internal WL mass calibration. However, even when analyzing the same data combination used in dH16 (without WL data) and applying the same priors, our analysis pipeline gives a more negative value of $w = -1.53^{+0.36}_{-0.25}$. As described in Section 3.4, we have extensively tested our analysis pipeline, including tests against mock catalogs with input values of $w \neq -1$. The analysis pipeline used in dH16 was not subjected to that test. Using our internal WL mass calibration shifts the constraints on w toward even more negative values. Finally, the cluster photometric redshifts were updated since the dH16 analysis (see Section 2.1), with the net impact being a shift in w toward less negative values of similar magnitude to the shift due to our WL mass calibration. In the end, some of these shifts
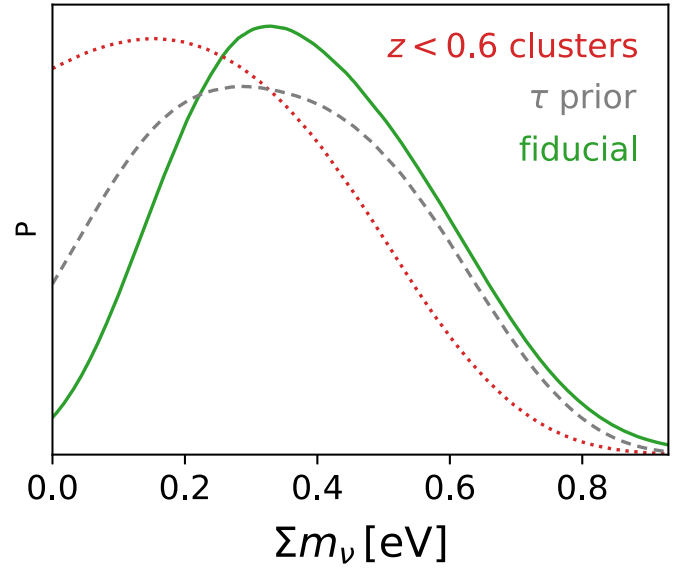
Figure 10. Constraints on $\sum m_\nu$ from the joint analysis of SPTcl and *Planck* data. Our fiducial analysis favors a nonzero sum of neutrino masses. However, when only using the low-redshift half $z < 0.6$ of our cluster sample or when replacing *Planck* TT+lowTEB with *Planck* TT + a prior $\tau \sim \mathcal{N}(0.054, 0.007^2)$, this preference diminishes.
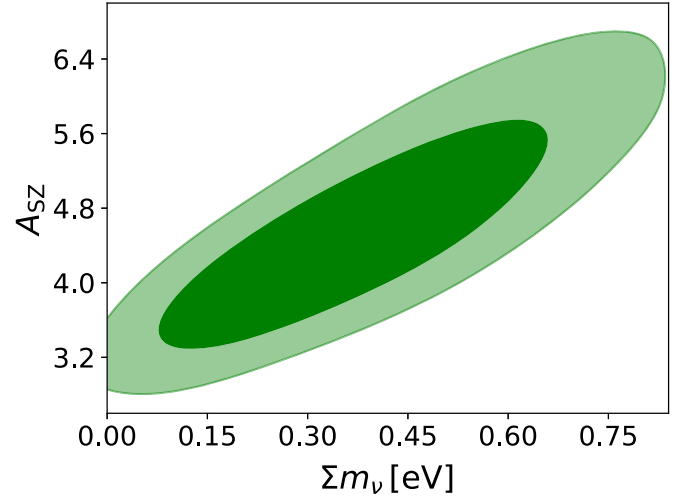

Figure 11. Parameter correlation between the sum of neutrino masses $\sum m_\nu$ and the amplitude of the SZ observable–mass relation A_{SZ} for the SPTcl+*Planck* data set. An improved cluster mass calibration will enable tighter constraints on neutrino properties.

in w partially cancel out, and the final constraint we present here is 0.7σ low in comparison to that in dH16.

We proceed and analyze the joint SPTcl+*Planck* data set. The cluster data break some of the *Planck* parameter degeneracies shown in Figure 12, and we measure

$$w = -1.12 \pm 0.21 \tag{49}$$
$$\Omega_m = 0.347 \pm 0.039 \tag{50}$$
$$\sigma_8 = 0.761 \pm 0.027 \tag{51}$$
$$\sum m_\nu = 0.50 \pm 0.24 \text{ eV.} \tag{52}$$

Interestingly, while the individual constraints on w are both centered on $w \approx -1.5$, the joint analysis provides a constraint that is offset closer toward $w = -1$. This is due to the different
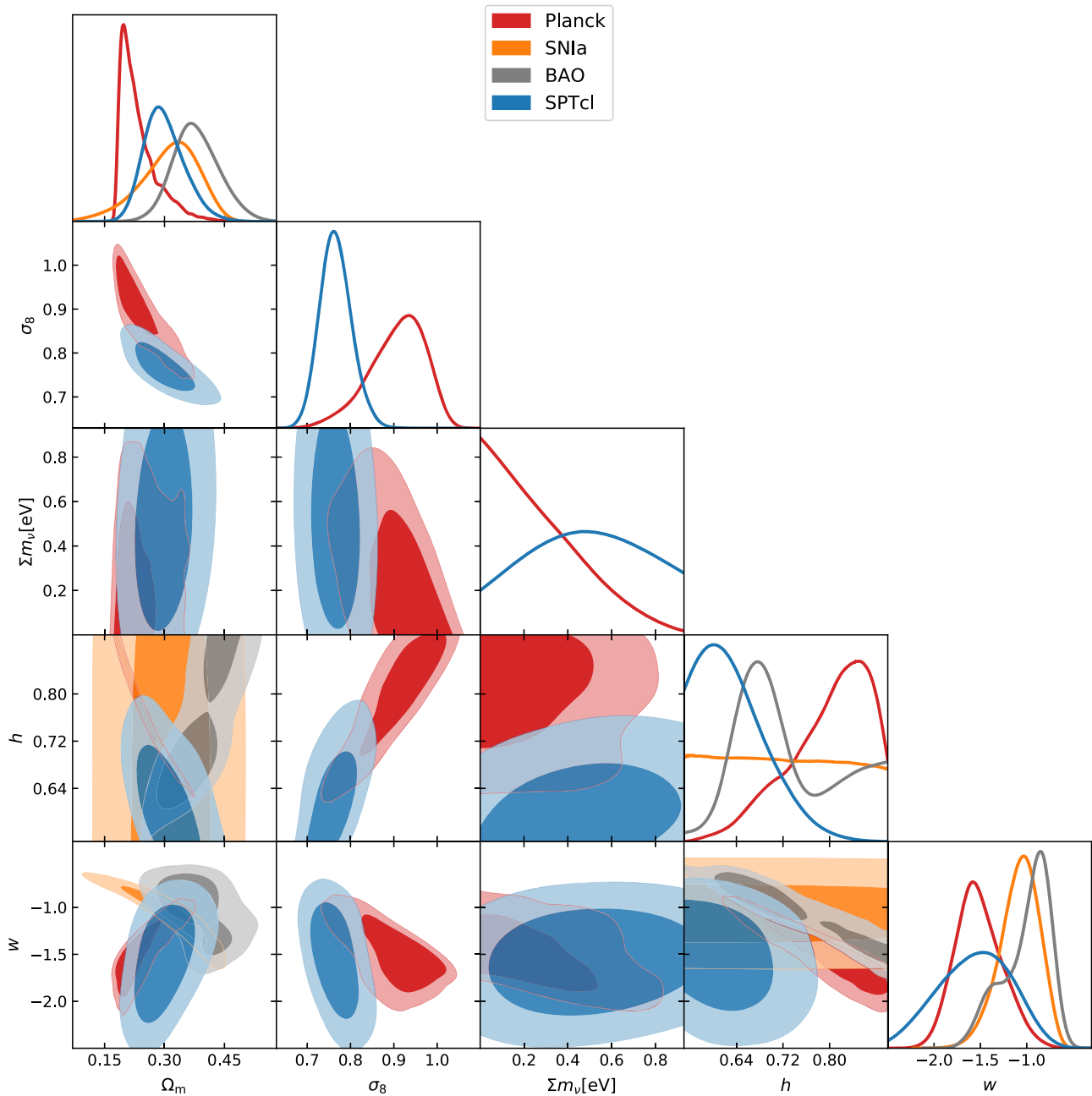
Figure 12. Constraints on νwCDM from SPT clusters, *Planck*, BAO, and SNe Ia. The 95% credibility contours all overlap. The biggest differences appear between SPTcl and *Planck* in the σ_8 and h parameters.

orientations of the $w - \sigma_8$ degeneracies in Figure 12 that overlap close to $w = -1$. Compared to the results obtained in $\nu\Lambda$CDM, the constraints on σ_8 and $\sigma_8(\Omega_{\rm m}/0.3)^{0.2}$ do not degrade. However, the constraining power on the remaining cosmological parameters weakens (see Table 3).

Figure 12 further shows the constraints obtained from BAOs and SNe Ia. Neither of the two are affected by σ_8 and $\sum m_\nu$.[58]

___

[58] We note an unexpected shape of the BAO posterior on h, with a peak at $h \approx 0.68$ and a rising tail toward the edge of the prior $h < 0.9$. This is caused by the subsamples of BAOs providing different results: The 6dF+SDSS posterior peaks at $h \approx 0.68$ and exhibits an approximately flat, nonzero tail in the range $0.8 < h < 0.9$. The posterior from BOSS increases monotonically throughout the entire allowed range in h and peaks at $h = 0.9$. Therefore, the joint BAO data set peaks at the 6dF+SDSS location but then rises again toward $h = 0.9$ owing to the BOSS constraint.

However, they both exhibit narrow parameter degeneracies that cut through the region of parameter space that is allowed by *Planck*. Therefore, the joint analyses of *Planck*+BAO and *Planck*+SN Ia allow for constraints on νwCDM that are tighter than the ones from *Planck*+SPTcl (see Figure 13).

Finally, we analyze the joint *Planck*+BAO+SN Ia+SPTcl data set (see constraints in Table 3). In comparison to *Planck* +BAO+SN Ia, the addition of the SPTcl data set leads to a shift $\Delta\sigma_8 = -0.031$. The constraints on $\Omega_{\rm m}$, h, and w are negligibly affected. However, note that the 95% upper limit on $\sum m_\nu$ from *Planck*+BAO+SN Ia increases by 63% when adding SPTcl. A similar effect was seen in the DES 3×2 pt analysis (Abbott et al. 2018), where the upper limit on $\sum m_\nu$ from *Planck*+BAO+SN Ia increased by a similar amount when adding the DES data. Both effects are due to the lower
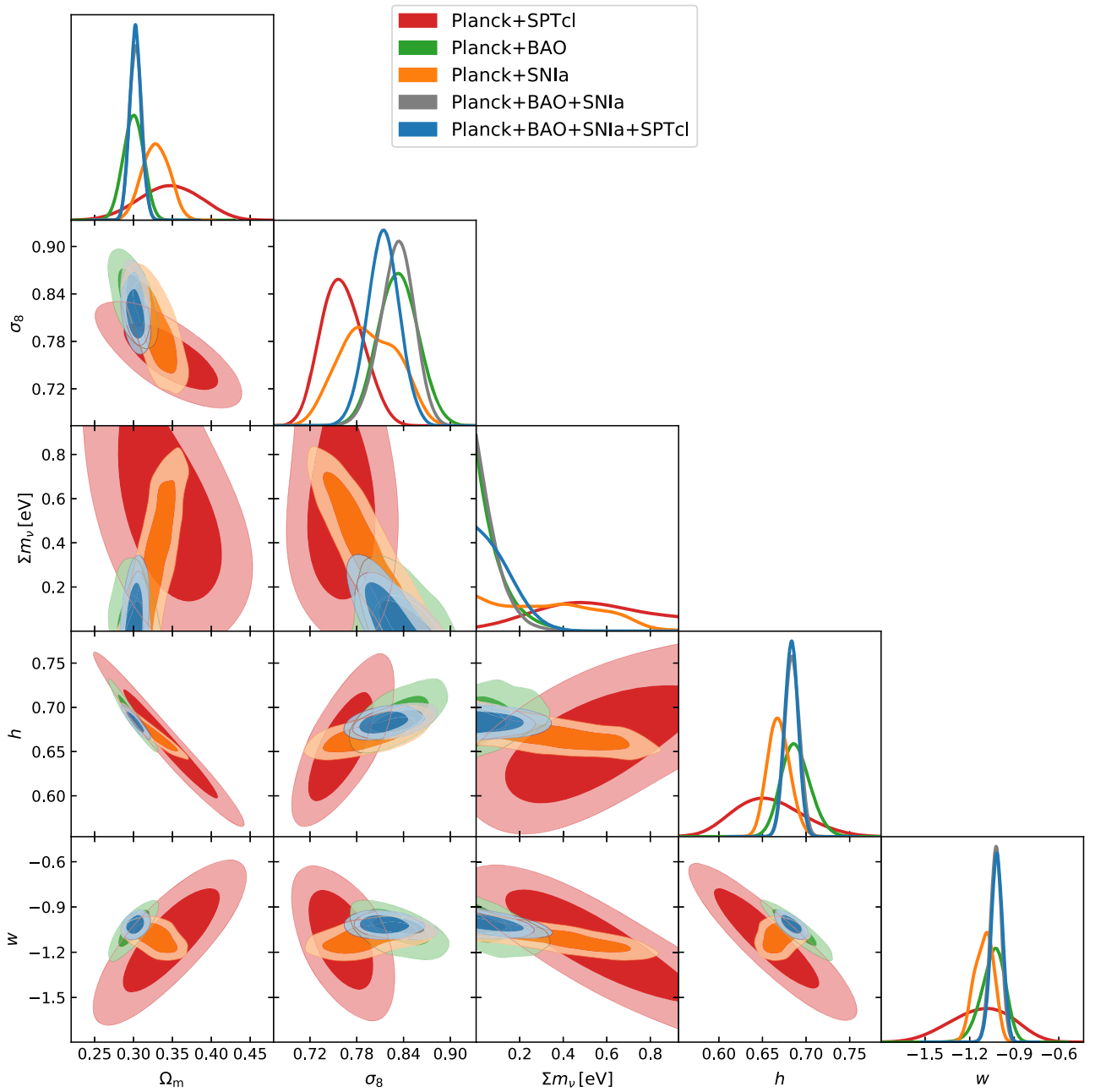
Figure 13. Constraints on νwCDM from joint analyses of *Planck* with SPTcl, BAOs, or SNe Ia. We also show *Planck*+BAO+SN Ia and the full joint analysis *Planck*+BAO+SN Ia+SPTcl. When combining with *Planck*, our cluster data set does not contribute as much additional information as do the other two external probes BAOs and SNe Ia.

clustering amplitude measured by SPTcl and DES relative to the prediction by *Planck*+BAO+SN Ia.

4.3.1. νwCDM: Robustness of Our Results to Data Cuts

In Appendix C (Figure 17), we show the parameter constraints that we recover when cutting our cluster sample in half at redshift 0.6, or when choosing a higher SZ selection threshold $\xi > 6.5$. There are no significant departures from our fiducial results for any data subset. However, both the low-redshift half of the data and the subsample above $\xi > 6.5$ yield constraints on w that are closer to the cosmological constant $w = -1$:

$$w(0.25 < z < 0.6) = -1.01^{+0.41}_{-0.25} \qquad (53)$$

$$w(\xi > 6.5) = -1.21^{+0.42}_{-0.29}. \qquad (54)$$

Conversely, the high-redshift half of the data gives

$$w(z > 0.6) = -1.58 \pm 0.46. \qquad (55)$$

We note that the constraints on w from the full sample are quite similar to this constraint from the high-redshift half of the data.

Figure 17 further shows a strong degeneracy between w and the redshift evolution parameters of the scaling relations C_{SZ} and C_{Y_X}. To tighten the dark energy constraints in future analyses, it will therefore be important to improve the mass calibration over the entire redshift range of the cluster sample.

4.4. Growth of Structure: Measuring $\sigma_8(z)$

We consider another extension to ΛCDM where we do not alter the background expansion but change the growth of structure. Clusters have been used to constrain modified structure growth by, for example, fitting for the growth index γ, which is defined by the relation $d\ln\delta/d\ln a \equiv \Omega_m^\gamma(a)$ (e.g., Peebles 1980). A value of $\gamma \approx 0.55$ corresponds approximately to the growth rate in ΛCDM, and clusters allow for constraints on γ at the $\sim$40% level (e.g., Rapetti et al. 2013; Bocquet et al. 2015; Mantz et al. 2015).

Instead of modeling linear deviations from GR via the growth index, we pursue a different route and constrain the growth of structure by directly measuring the linear amplitude of the density fluctuations, σ_8, as a function of redshift. We can then compare the measured $\sigma_8(z)$ with predictions from $\nu\Lambda$CDM, νwCDM, and more exotic models. This approach is nonparametric in that it does not assume a specific description for modified growth of structure, but rather assumes a $\nu\Lambda$CDM model (with its parameters allowed to vary) within each redshift bin.

We start from the $\nu\Lambda$CDM model and modify the amplitude of the linear matter power spectrum $P(k, z)$ within different redshift bins. We introduce an additional model parameter $\sigma_8(z_i)$ in each bin and normalize $P(k, z)$ within each redshift bin i to match $\sigma_8(z_i)$. The HMF is then computed from the modified $P(k, z)$ in the usual way. We define four redshift bins such that all bins contain approximately equal numbers of SPT clusters. We choose bin limits ($z = 0.25, 0.45, 0.6, 0.75, 1.7$). We include *Planck* primary CMB data in the fit. By construction, in our model the *Planck* data only constrain the background cosmology (expansion history $E(z)$), but they do not contribute to constraining $\sigma_8(z)$. For simplicity, we do not use any X-ray data here and thus use the joint SPT-SZ+WL+*Planck* data set; we apply the simulation prior on the SZ scatter.

We explore two scenarios: (i) We assume our fiducial SZ scaling relation model across the entire redshift range. This means that the mass calibration will be correlated across the four redshift bins. (ii) We additionally introduce independent normalizations of the SZ scaling relation $A_{SZ,i}$ in each redshift bin i. This way, the amplitude of the SZ scaling relation is independently determined in each redshift bin (up to the shared WL systematics that are, however, subdominant here given the low number of clusters with WL constraints). We call the first scenario "coupled" and the second "decoupled," in reference to the treatment of the normalization of the SZ observable–mass relation.

Constraints on A_{SZ} and $\sigma_8(z)$ for the coupled and decoupled analyses are shown in Table 4. In the coupled analysis, the four measurements of $\sigma_8(z)$ are quite correlated with correlation coefficients $\rho(\sigma_8(z)) = 0.55$–0.60 because they are limited by the uncertainty in the observable–mass scaling relation that is shared across the entire redshift range. In the decoupled analysis, however, the $\sigma_8(z)$ parameters are much less correlated ($\rho(\sigma_8(z)) = 0.06$–0.12), as mass calibration in each bin is done almost independently, and each $\sigma_8(z_i)$ is mostly degenerate with the corresponding normalization parameter $A_{SZ}(z_i)$. As expected, the decoupled analysis leads to weaker constraints.

In Figure 14, we show measurements of σ_8 as a function of redshift. The red band shows the prediction for $\sigma_8(z)$ assuming $\nu\Lambda$CDM and *Planck* cosmological parameters. Blue and orange data points show measurements of $\sigma_8(z)$ using our clusters (with *Planck* priors on the background cosmology). The cluster measurements are all slightly lower than the predictions using *Planck* data, which simply reflects the difference in σ_8 discussed above for the $\nu\Lambda$CDM model (see Figure 9). We

emphasize that this offset is roughly constant throughout the entire range in redshift. In particular, the two bins above $z > 0.6$ that are leading to some shifts in cosmology and scaling relations as described in earlier sections do not seem to provide constraints that are qualitatively different from those obtained from the low-redshift bins.

Our measurements of $\sigma_8(z)$ are limited by the determination of A_{SZ}, especially in the "decoupled" analysis. The three low-redshift bins will benefit from including cluster WL data from the Dark Energy Survey (M. Paulus et al. 2019, in preparation). The highest-redshift bin can only be improved with deep, high-resolution WL data, e.g., from *HST*, or with lensing information from the CMB (e.g., Baxter et al. 2018). On the other hand, our cluster sample, together with this technique, allows us to place competitive constraints on the growth of structure over a wide range in redshifts.

4.5. Implications for SZ-based Cluster Halo Masses

For the $\nu\Lambda$CDM and νwCDM analyses discussed above, Table 3 also presents constraints on the SZ scaling relation parameters. These, together with Equations (1) and (8), allow one to compute mass estimates $P(M_{500c}|\xi, z, \boldsymbol{p})$ for each cluster in our sample. Moreover, the scaling relation parameter constraints provide another point of comparison with past analyses.

The results in Table 3 exhibit a range of parameters across the six different analyses, but in no case are the parameter differences statistically significant. This indicates that the best estimates of the cluster masses are consistent among the different combinations of data and within the different cosmological models. As an example, the addition of the *Planck* data set as an external prior leads to preferred values of the amplitude parameter A_{SZ} that are lower, corresponding to $\sim$8% and $\sim$4% higher masses at the pivot in $\nu\Lambda$CDM and νwCDM, respectively. These mass shifts are smaller than those presented by Bocquet et al. (2015), where the impact of external priors was first discussed. Interestingly, the redshift slope C_{SZ} prefers higher values in the νwCDM model, which corresponds to high-redshift masses that are smaller relative to clusters with the same ξ at low redshift. In the νwCDM model these same values of $C_{SZ} \sim 1$ are preferred with or without *Planck* priors but shift back to a lower value when BAO+SN Ia constraints are added. In comparison, in the results for ΛCDM presented in Table 3 of dH16, the amplitude parameter for the SPTcl+*Planck*+BAO analysis was $A_{SZ} = 3.53 \pm 0.27$, which is significantly lower than the values presented here. Note, however, that massive neutrinos were not marginalized over in the baseline analysis in dH16.

Given the consistency in the implied masses across all six analyses presented here, we adopt the $\nu\Lambda$CDM results for the baseline SPTcl data set in calculating mean masses and mass uncertainties (Table 3, Column (3)). The mass uncertainties include the ξ measurement and intrinsic scatter uncertainties (together these correspond to $\sim$20% uncertainty for a cluster near our selection threshold), as well as marginalization over the posterior parameter distributions for A_{SZ}, B_{SZ}, C_{SZ}, and $\sigma_{\ln\zeta}$ and over the cosmological parameters (this corresponds to an additional $\sim$15% uncertainty due to the remaining uncertainties in the mass calibration of the SPT-SZ sample). These masses are calculated by sampling the distribution

$$P(M|\xi, z, \boldsymbol{p}) = \iint dM d\zeta P(\xi|\zeta) P(\zeta|M, z, \boldsymbol{p}) P(M|z, \boldsymbol{p}) \quad (56)$$

at each step in the likelihood analysis.

Table 4
Constraints on σ_8 and the SZ Scaling Relation Normalization A_{SZ} as a Function of Redshift, Measured in Four Redshift Bins

Parameter	Coupled Analysis	Decoupled Analysis	*Planck*(TT+lowTEB)
A_{SZ}	$5.40^{+0.80}_{-1.15}$	...	...
$A_{SZ}(0.25 < z < 0.45)$	...	$4.90^{+0.88}_{-1.09}$	...
$A_{SZ}(0.45 < z < 0.6)$	...	$10.29^{+2.56}_{-4.23}$	...
$A_{SZ}(0.6 < z < 0.75)$	...	$7.29^{+1.66}_{-4.47}$	...
$A_{SZ}(0.75 < z < 1.7)$	...	$10.63^{+2.19}_{-3.08}$	...
$\sigma_8(z = 0.35)$	0.592 ± 0.031	0.609 ± 0.028	0.656 ± 0.029
$\sigma_8(z = 0.525)$	0.543 ± 0.029	0.484 ± 0.034	0.597 ± 0.028
$\sigma_8(z = 0.675)$	0.519 ± 0.026	0.505 ± 0.046	0.555 ± 0.026
$\sigma_8(z = 1.225)$	0.415 ± 0.023	0.371 ± 0.020	0.432 ± 0.021
$\rho(\sigma_8(z))$	0.55–0.60	0.06–0.12	...

Note. In the coupled analysis we assume a single A_{SZ} parameter. In the decoupled analysis we fit for A_{SZ} separately in each redshift bin; this decorrelates the measurements of $\sigma_8(z)$ as evidenced by $\rho(\sigma_8(z))$.

Table 5 contains a list of all cluster candidates in our sample with the associated sky location, SPT detection significance ξ, redshift, and halo mass M_{500c}. In addition, we present the mass M_{200c} for each system, assuming the concentration–mass relation from Duffy et al. (2008).

5. Summary and Outlook

We present an analysis of the SPT-SZ cluster sample, supplemented with optical WL data and X-ray Y_X measurements. We set up a self-consistent analysis framework in which cosmology, scaling relations, a possible correlated scatter among cluster mass proxies, and other nuisance parameters are fit simultaneously. Within this framework, the WL data are used to constrain the normalization of the observable–mass relations (at various redshifts and cluster masses). We use numerical simulations to calibrate the relation between the unobserved, true halo mass and the observed radial WL shear profiles. Wide, noninformative priors are assumed on the parameters of the SZ and X-ray scaling relations. At present, our mass calibration is limited by the number of clusters with WL data; the systematic uncertainties in the WL analysis are subdominant with 5.6% in mass for our ground-based data and 9.2%–9.4% for the *HST* sample (S18; D19).

Our main findings are as follows:

1. Assuming simulation-based priors on the relation between true mass and WL mass M_{WL}, we are able to simultaneously fit for cosmology (constraining Ω_m, σ_8, w) while constraining the amplitudes, mass slopes, redshift evolutions, and intrinsic scatter of the SZ and X-ray observable–mass relations. We marginalize over flat priors on $\Omega_\nu h^2$, $\Omega_b h^2$, n_s, and h that are not constrained from cluster data alone.

2. Assuming the $\nu\Lambda$CDM model, our cluster-based constraint on $\sigma_8(\Omega_m/0.3)^{0.2} = 0.766 \pm 0.025$ is lower than the one obtained from primary CMB fluctuations by *Planck*. The agreement between the two measurements is $p = 0.28$, or 1.1σ.

3. We constrain the redshift evolution of the X-ray Y_X–mass relation to $C_{Y_X} = -0.31^{+0.14}_{-0.21}$ and the redshift evolution of the M_{gas}–mass relation to $C_{M_g} = -0.05 \pm 0.17$. The self-similar evolution -0.4 for Y_X–mass and 0 for M_{gas}–mass is encompassed in the 1σ interval in both cases.

4. We find the mass dependence of the X-ray Y_X–mass relation $B_{Y_X} = 0.514 \pm 0.037$ to be steeper than the self-similar expectation $B_{Y_X} = 0.6$ with a *p*-value of $p = 0.021$ (2.3σ). Interestingly, this difference is resolved when we only consider the low-redshift half of our sample at $z < 0.6$, where we measure $B_{Y_X} = 0.583^{+0.054}_{-0.069}$. Conversely, the high-redshift half of our sample favors a steeper slope $(B_{Y_X} = 0.503^{+0.037}_{-0.047})$; see also Figure 8. The slope of the M_{gas}–mass relation $B_{M_g} = 1.22 \pm 0.07$ is also steeper than the self-similar evolution $B_{M_g} = 1$. Here as well, the measurement of B_{M_g} at low redshift below $z = 0.6$ is closer to the self-similar value $(B_{M_g} = 1.12 \pm 0.09)$ than the high-redshift measurement $(B_{M_g} = 1.36 \pm 0.11)$.

5. The joint data set combining our clusters and primary CMB measurements from *Planck* allows for a constraint on the sum of neutrinos masses $\sum m_\nu = 0.39 \pm 0.19$ eV $(\sum m_\nu < 0.74$ eV (95% C.L.)). This preference for a nonzero sum of neutrino masses diminishes when combining *Planck* with only the low-redshift $(z < 0.6)$ half of our cluster sample or when adopting a lower value of τ as suggested by Planck Collaboration et al. (2018a). Due to parameter degeneracies, an improved cluster mass calibration will directly translate into tighter constraints on neutrino masses.

6. Our constraint on $w = -1.55 \pm 0.41$ is somewhat lower than a cosmological constant, with $p = 0.076$ (1.8σ). The SPTcl contours in the Ω_m–σ_8–w space are closed; see Figure 12. This reflects the fact that our cluster sample is able to constrain the three parameters simultaneously. When only considering the high-redshift $z > 0.6$ subsample, we obtain $w = -1.58 \pm 0.46$, whereas we obtain a less negative constraint $w = -1.01^{+0.41}_{-0.25}$ from the low-redshift subsample at $0.25 < z < 0.6$.

7. We employ a new approach to measuring the linear growth of structure using clusters. This allows us to track the evolution of structure growth since redshift $z \sim 1.7$. Figure 14 shows that structure formation evolved in agreement with the $\nu\Lambda$CDM prediction, although with a somewhat lower amplitude than predicted assuming cosmological parameters from *Planck*.

The validity of our cluster-based constraints relies on an accurate prediction of the HMF throughout the entire parameter space considered. However, the HMF fit by Tinker et al. (2008) is calibrated using N-body simulations for cosmologies that are close to *WMAP* results, and the extrapolation to other cosmologies is performed assuming the universality of the
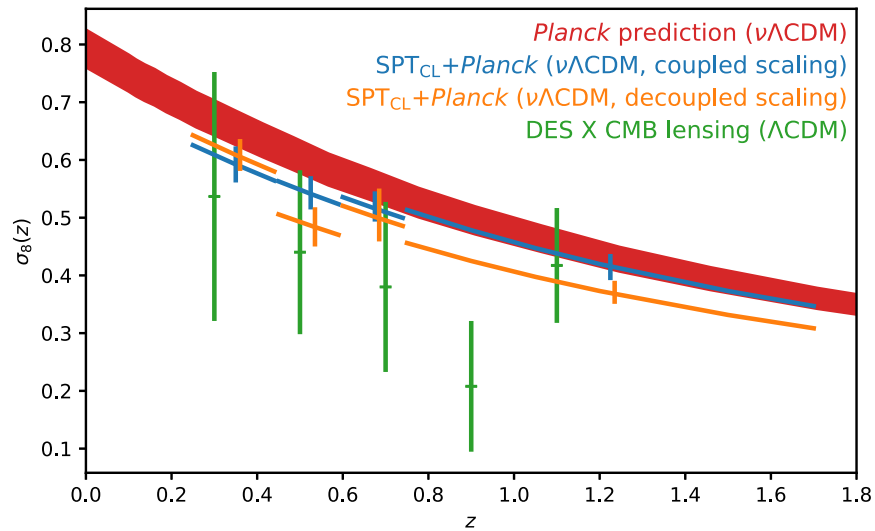
Figure 14. Evolution of σ_8 as a function of redshift. The red band shows the 1σ interval of the prediction obtained from *Planck* in the $\nu\Lambda$CDM cosmology. The blue data points are obtained in a joint SPTcl+*Planck* analysis, where $\sigma_8(z)$ is constrained only by the cluster sample. Orange data points are obtained from a similar analysis that allows for more freedom in the SZ scaling relation (see Section 4.4). The nearly horizontal error bars on the blue and orange data points indicate the extent of the redshift bins and are shaped to follow the evolution of σ_8 in the $\nu\Lambda$CDM model. For comparison, green data points show constraints from the cross-correlation of the galaxy density in the Dark Energy Survey Science Verification data with CMB lensing from SPT (Giannantonio et al. 2016).

Table 5
Galaxy Cluster Candidates with $\xi > 4.5$ in the SPT-SZ Survey

SPT ID	R.A. (J2000)	Decl. (J2000)	ξ	θ_c (arcmin)	Y_{SZ} (10^{-6} arcmin^{-2})	Redshift	M_{500c} ($10^{14}\,M_\odot/h_{70}$)	M_{200c} ($10^{14}\,M_\odot/h_{70}$)	$M_{500c}^{\text{no syst.}}$ ($10^{14}\,M_\odot/h_{70}$)
SPT-CL J0000-4356	0.0663	−43.9494	5.92	0.25	77 ± 21	0.73 ± 0.05*	$3.55^{+0.65}_{-0.83}$	$5.56^{+1.04}_{-1.34}$	$4.01^{+0.67}_{-0.74}$
SPT-CL J0000-5748 [WL,X]	0.2499	−57.8064	8.49	0.50	83 ± 13	0.702	$4.33^{+0.65}_{-0.86}$	$6.79^{+1.04}_{-1.37}$	$4.88^{+0.59}_{-0.71}$
SPT-CL J0001-4024	0.3610	−40.4108	5.42	0.75	60 ± 13	0.83 ± 0.03*	$3.19^{+0.65}_{-0.83}$	$5.03^{+1.04}_{-1.33}$	$3.62^{+0.64}_{-0.73}$
SPT-CL J0001-4842	0.2768	−48.7132	5.69	1.25	78 ± 13	0.33 ± 0.02*	$3.89^{+0.75}_{-0.90}$	$5.92^{+1.16}_{-1.40}$	$4.48^{+0.75}_{-0.83}$
SPT-CL J0001-5440	0.4059	−54.6697	5.69	1.00	60 ± 13	0.82 ± 0.08*	$3.47^{+0.64}_{-0.88}$	$5.46^{+1.02}_{-1.42}$	$3.88^{+0.67}_{-0.75}$
SPT-CL J0001-6258	0.4029	−62.9808	4.69	1.50	52 ± 16	0.21 ± 0.02	$3.32^{+0.66}_{-0.88}$	$4.97^{+1.00}_{-1.34}$	$3.89^{+0.65}_{-0.87}$
SPT-CL J0002-5224	0.6433	−52.4092	4.67	1.00	48 ± 13	>0.71	⋯	⋯	⋯
SPT-CL J0002-5557	0.5138	−55.9621	5.20	0.25	55 ± 18	1.15 ± 0.10	$2.84^{+0.58}_{-0.81}$	$4.55^{+0.95}_{-1.32}$	$3.20^{+0.56}_{-0.68}$
SPT-CL J0003-4155	0.7842	−41.9307	4.75	0.25	59 ± 20	>0.76	⋯	⋯	⋯
SPT-CL J0007-4706	1.7514	−47.1159	4.55	0.75	58 ± 13	0.46 ± 0.04*	$3.14^{+0.62}_{-0.85}$	$4.80^{+0.96}_{-1.33}$	$3.65^{+0.58}_{-0.83}$

Note. The subsample with $\xi \geqslant 5$ and $z \geqslant 0.25$ is used in the cosmological analysis. Clusters with follow-up WL and/or X-ray data that we use in this work are marked with "WL" and/or "X." The positions ξ, core radii θ_c, and Y_{SZ} are the same as presented in Bleem et al. (2015), while the redshifts marked with an asterisk have been updated. Spectroscopic redshifts are quoted without uncertainties. The mean mass estimates and mass uncertainties take the intrinsic and measurement scatter into account. We quote redshift lower limits for unconfirmed SZ detections. The mass estimates M_{500c} and M_{200c} are derived from the SPTcl data set in the $\nu\Lambda$CDM model (Table 3, Column (3)) and are fully marginalized over cosmology and scaling relation parameter uncertainties. The estimates $M_{500c}^{\text{no syst.}}$ are computed assuming a fixed cosmology and using the best-fit scaling relation parameters obtained from fitting the SPT-SZ number counts against that fixed cosmology (this approach was also adopted in Bleem et al. 2015). The catalog can also be found at https://pole.uchicago.edu/public/data/sptsz-clusters.

(This table is available in its entirety in machine-readable form.)

HMF. Ongoing analyses of cosmological simulations will provide accurate predictions of the HMF for a much broader range of cosmologies (Heitmann et al. 2016; McClintock et al. 2019a, S. Bocquet et al. 2019, in preparation).

We discuss the departure from self-similarity of the X-ray Y_X and M_{gas} mass slopes. There is a suggestion of an evolution of the Y_X mass slope with redshift, where it exhibits more self-similar results in the low-redshift half cluster sample. Similar results have been presented in the previous SPT cosmology analysis (dH16), as well as in X-ray observable–mass scaling relation studies that rely on SZ-based cluster masses (Chiu et al. 2016, 2018; Bulbul et al. 2019), where masses are calculated using the mass calibration results from previous SPT cluster cosmology analyses (Bocquet et al. 2015, dH16). This could be a sign that X-ray scaling relations

depart from self-similarity in this mass and redshift range (e.g., the ICM mass fraction varies with cluster mass as shown first in Mohr et al. 1999), or there could be additional effects not captured by our model that affect, e.g., the SZ scaling relation or selection. Larger SZ-selected cluster samples and more extensive follow-up data are necessary to discern these effects.

In upcoming analyses, we will expand our SPT-SZ cluster sample with data from SPTpol. This will both increase our sample of high-mass clusters and push down to lower cluster masses in the deeper fields of the survey. At the same time, it is important to pursue our WL campaign at all redshifts covered by our sample. Indeed, the strategic overlap with the DES (Dark Energy Survey Collaboration et al. 2016) will allow for a robust mass calibration at moderate redshifts (Melchior et al. 2017;
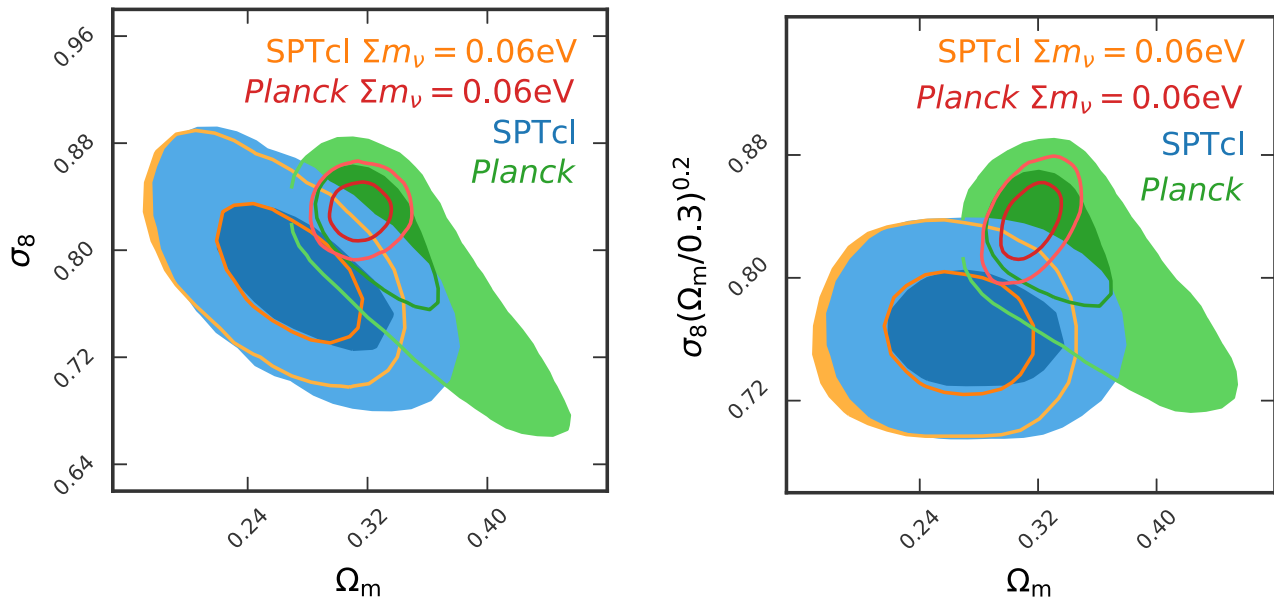
Figure 15. Impact of marginalization over $\Omega_\nu h^2$: the cluster constraints are weakly affected, whereas the *Planck* constraints significantly tighten when $\Omega_\nu h^2$ is fixed. Nevertheless, the level of (dis)agreement between these data sets is not substantially changed by marginalizing over $\Omega_\nu h^2$.

McClintock et al. 2019b; Stern et al. 2019). To exploit the full potential of the SPT cluster sample, it will be crucial to also tighten the WL mass constraints at higher redshifts. At intermediate redshifts this can be achieved with deep ground-based K_s imaging (Schrabback et al. 2018b), but at high redshifts $z > 1$ these measurements critically require additional *HST* observations or ultimately the data sets from Euclid (Laureijs et al. 2011) and LSST (Ivezic et al. 2008). With the current and next generation of high-resolution CMB experiments such as SPT-3G (Benson et al. 2014; Bender et al. 2018), Advanced ACTpol (De Bernardis et al. 2016), or CMB-S4 (Abazajian et al. 2016), CMB lensing will provide another means of accurate mass calibration out to redshifts well beyond $z \sim 1$.

Appendix A
Impact of Marginalization over the Sum of Neutrino Masses

Our baseline analysis is carried out marginalizing over the sum of neutrino masses (by allowing $\Omega_\nu h^2$ to vary in the range 0–0.01). In Figure 15, we show that instead fixing the sum of neutrino masses to the minimum allowed value from oscillation experiments (0.06 eV, corresponding to $\Omega_\nu h^2 = 6.5 \times 10^{-4}$) does not qualitatively change the constraints in the Ω_m–σ_8 space from our SPTcl data set. However, as is well known, the constraints from *Planck* tighten significantly when $\Omega_\nu h^2$ is fixed. We note that this tightening does not significantly affect the agreement between the two probes.

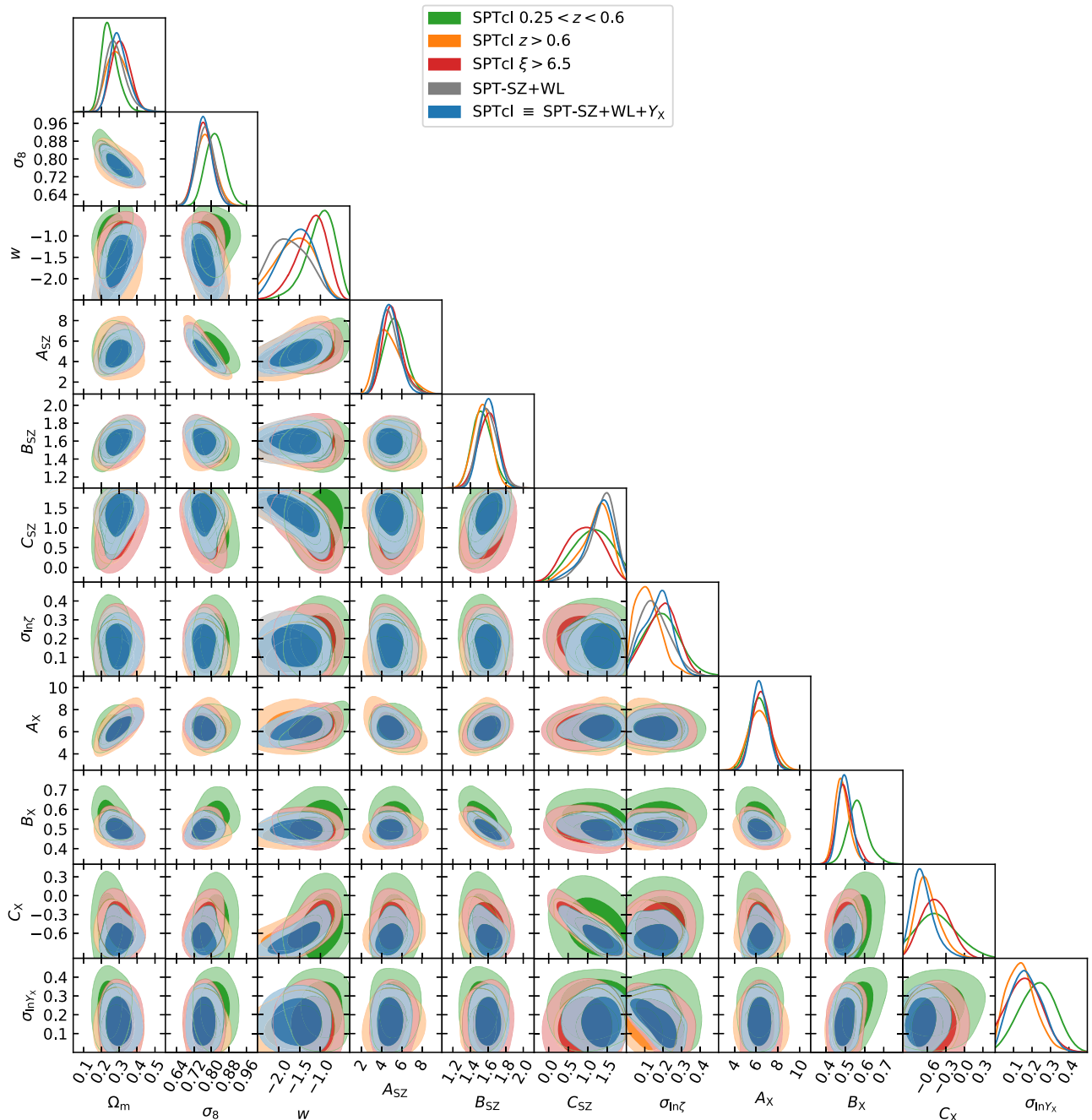[59] https://github.com/SebastianBocquet/pygtc
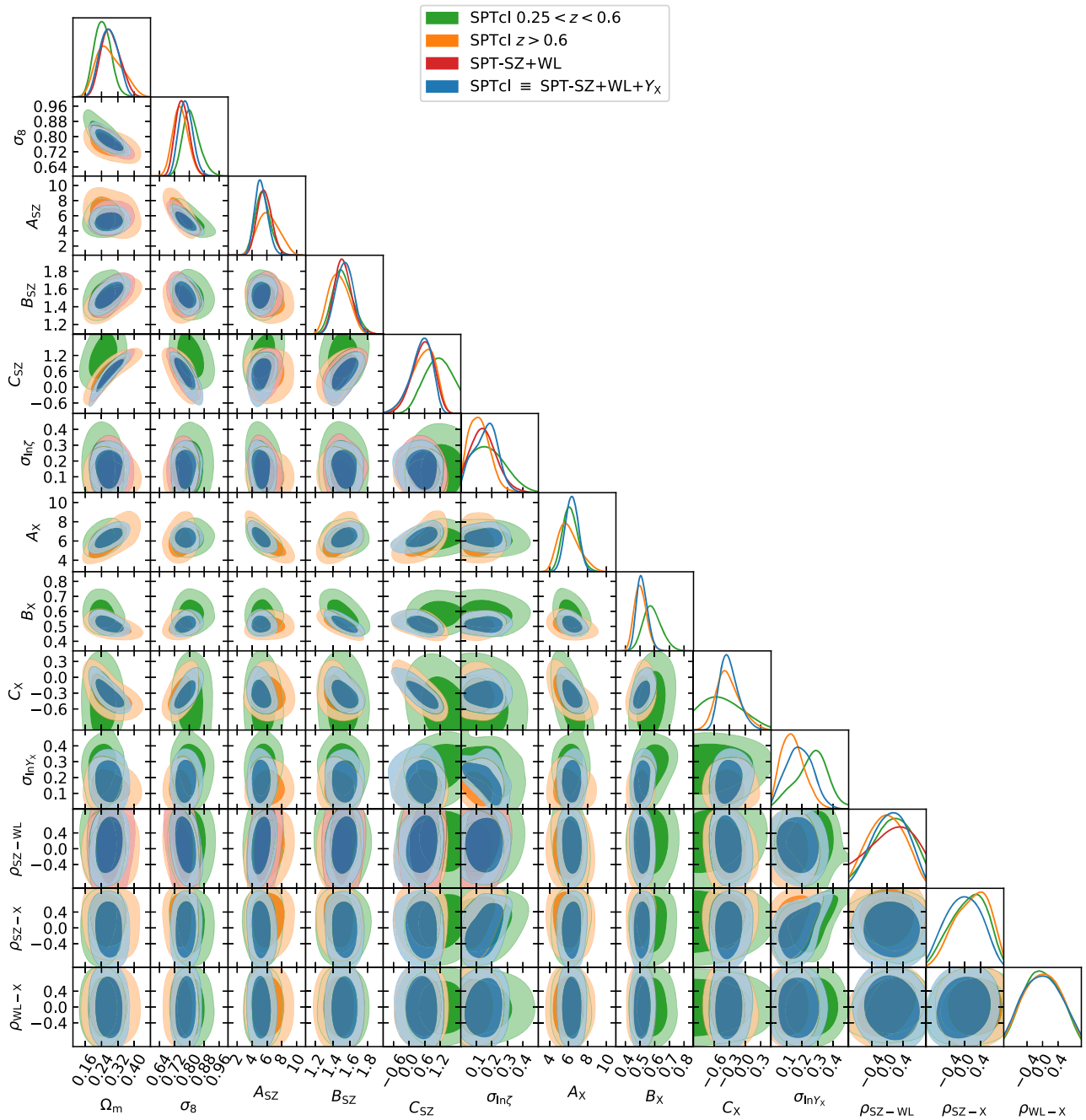
Figure 16. $\nu\Lambda$CDM constraints on a subset of cosmology and scaling relation parameters. The full set of fit parameters is listed in Table 2. Blue contours are obtained from the SPTcl (SPT-SZ+WL+Y_X) data set, green contours are obtained using all clusters in the redshift range $0.25 < z < 0.6$, orange contours are obtained from the high-redshift counterpart $z > 0.6$, and red contours are obtained using SPT-SZ+WL, without any X-ray data, but with a Gaussian prior applied on $\sigma_{\ln\zeta}$. The inclusion of X-ray does not lead to improved cosmological constraints, but allows us to drop the prior on scatter $\sigma_{\ln\zeta}$ and to constrain the X-ray scaling relation. Our current data set is not able to constrain any of the correlated scatter coefficients ρ. The visual impression that the ρ parameters are constrained is mostly due to the prior that the covariance matrix must be positive definite.

Appendix B
ΛCDM Results: Robustness to Splits in Redshift and Impact of X-Ray Data

Our baseline results are obtained from the SPTcl (SPT-SZ +WL+Y_X) data combination. Here we show the impact on scaling relation parameters and cosmology from different cuts. Figure 16 shows the most relevant subset of scaling relation and cosmological parameters for (i) the baseline analysis, (ii) an analysis of the low-redshift half of the cluster data ($0.25 < z < 0.6$), (iii) the high-redshift half of the sample

($z > 0.6$), and (iv) the SPT-SZ+WL data combination, without any X-ray data, but where an informative Gaussian prior is applied on the SZ scatter ($\sigma_{\ln\zeta} = \mathcal{N}(0.13, 0.13^2)$).

Importantly, the cosmological constraints on Ω_m–σ_8 are not much affected by the choice of subsample, and they only vary mildly along the degeneracy axis.

The low-redshift half of the sample only provides weak constraints on the redshift evolution of the X-ray scaling relation C_{Y_X}. We discussed the constraints on the X-ray mass slope B_{Y_X} in Section 4.1.5.

Figure 17. νwCDM constraints on a subset of cosmology and scaling relation parameters. The full set of fit parameters is listed in Table 2. Blue contours are obtained from the SPTcl (SPT-SZ+WL+Y_X) data set, green contours are obtained using all clusters in the redshift range $0.25 < z < 0.6$, orange contours are obtained from the high-redshift counterpart $z > 0.6$, red contours are obtained from the subsample of clusters above SPT detection significance $\xi > 6.5$, and gray contours are obtained using SPT-SZ+WL without any X-ray data, but with a Gaussian prior applied on $\sigma_{\ln \zeta}$. Both the low-redshift half of the sample and the $\xi > 6.5$ subsample favor a less negative w in better agreement with a cosmological constant.

Appendix C
wCDM Results: Robustness to Data Cuts and Impact of X-Ray Data

As in the previous section, here we discuss the impact of various data cuts on cosmological constraints, but this time in the context of the νwCDM model. Figure 17 shows the most relevant subset of scaling relation and cosmological parameters for analyses of (i) the baseline cluster sample, (ii) the low-redshift half of the cluster data ($0.25 < z < 0.6$), (iii) the high-redshift half of the sample ($z > 0.6$), (iv) a subsample selected above SPT detection significance $\xi > 6.5$, and (v) the SPT-SZ+WL data combination,

without any X-ray data, but where an informative Gaussian prior is applied on the SZ scatter ($\sigma_{\ln \zeta} = \mathcal{N}(0.13, 0.13^2)$).

As discussed above for the $\nu\Lambda$CDM analysis, we see some shifts in the X-ray slope B_{Y_X} and redshift evolution C_{Y_X}. The constraints on Ω_m and σ_8 are again not much affected by the choice of subsample. However, while not statistically significant, there are differences in the recovered values for w. Using the SPT-SZ+WL data combination provides the weakest constraint on w, and its posterior distribution is shifted toward more negative values, running against the hard prior at $w = -2.5$. Then, as already discussed in Section 4.3, both the low-redshift half of the
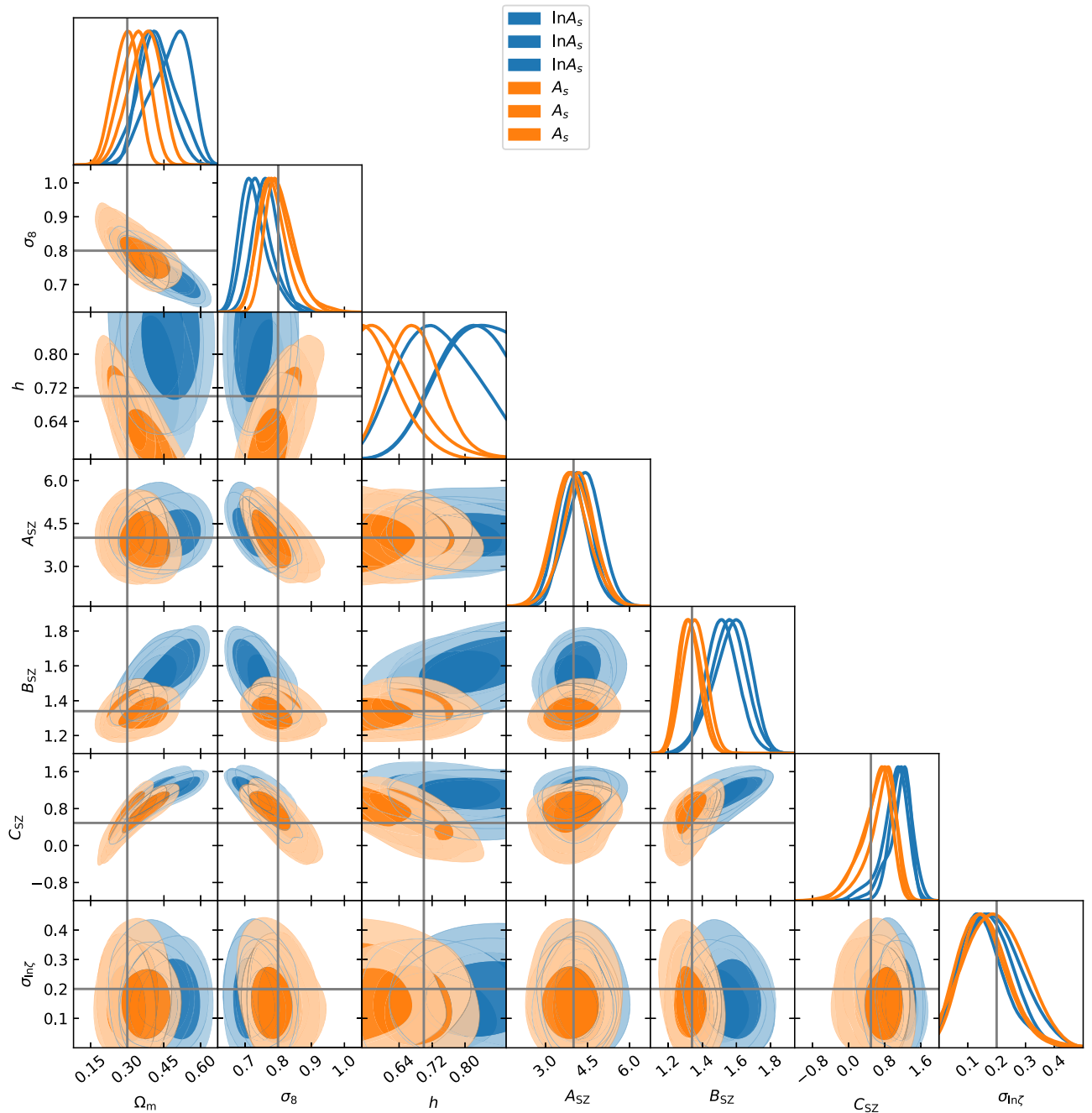
Figure 18. Constraints obtained running our analysis pipeline on three realizations of mock data. For simplicity, the mass calibration is replaced by Gaussian priors on $A_{SZ} = \mathcal{N}(4, 0.8^2)$ and $\sigma_{\ln\zeta} = \mathcal{N}(0.13, 0.13^2)$. Blue contours are obtained sampling from a flat prior on $\ln(10^{10}A_s) = 1$–4; orange contours are obtained sampling from a flat prior $A_s = 10^{-10}$–10^{-8}. The other parameters are sampled from flat priors. Solid lines show the mock catalog input parameters. Sampling from A_s performs better in terms of recovering the input values, and we choose this prior throughout this analysis.

sample and the higher-mass $\xi > 6.5$ subsamples prefer slightly higher w, with $w(z < 0.6) = -1.01^{+0.41}_{-0.25}$ and $w(\xi > 6.5) = -1.21^{+0.42}_{-0.29}$. The high-redshift half of the sample provides constraints $w(z > 0.6) = -1.58 \pm 0.46$ that are very similar to those from the full sample $w = -1.55 \pm 0.41$.
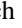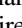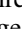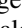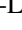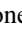
Appendix D
The Choice of Priors: Sampling from A_s versus Sampling from $\ln A_s$

In this work, we sample from a flat prior on A_s, following previous SPT analyses and, e.g., the DES Y1 analysis

(Abbott et al. 2018). In primary CMB studies, however, it is common practice to sample from $\ln 10^{10}A_s$. We test the impact of this choice of priors by analyzing mock catalogs sampling from a flat prior on either A_s or $\ln 10^{10}A_s$. Figure 18 shows that a flat prior on A_s performs better in terms of recovering the mock input parameters. This choice of prior does not matter in the limit where A_s (and/or $\ln 10^{10}A_s$) are tightly constrained, and we thus expect the impact of this prior choice to become less important as the constraining power of our data sets increases. Sampling from a flat prior on σ_8 instead produces results that are essentially identical to those obtained when sampling from $\ln 10^{10}A_s$.

ORCID iDs

S. Bocquet ⓘ https://orcid.org/0000-0002-4900-805X
J. P. Dietrich ⓘ https://orcid.org/0000-0002-8134-9591
D. E. Applegate ⓘ https://orcid.org/0000-0001-8322-4672
M. L. N. Ashby ⓘ https://orcid.org/0000-0002-3993-0745
M. Bayliss ⓘ https://orcid.org/0000-0003-1074-4807
M. Brodwin ⓘ https://orcid.org/0000-0002-4208-798X
T. M. Crawford ⓘ https://orcid.org/0000-0001-9000-5013
T. de Haan ⓘ https://orcid.org/0000-0001-5105-9473
W. R. Forman ⓘ https://orcid.org/0000-0002-9478-1682
G. P. Garmire ⓘ https://orcid.org/0000-0002-7371-5416
E. M. George ⓘ https://orcid.org/0000-0001-7874-0445
A. H. Gonzalez ⓘ https://orcid.org/0000-0002-0933-8601
J. Hlavacek-Larrondo ⓘ https://orcid.org/0000-0001-7271-7340
H. Hoekstra ⓘ https://orcid.org/0000-0002-0641-3231
G. Khullar ⓘ https://orcid.org/0000-0002-3475-7648
R. Kraft ⓘ https://orcid.org/0000-0002-0765-0511
A. von der Linden ⓘ https://orcid.org/0000-0002-3881-7724
D. P. Marrone ⓘ https://orcid.org/0000-0002-2367-1080
D. Rapetti ⓘ https://orcid.org/0000-0003-2196-6675
C. L. Reichardt ⓘ https://orcid.org/0000-0003-2226-9169
B. R. Saliwanchik ⓘ https://orcid.org/0000-0002-5089-7472
A. A. Stark ⓘ https://orcid.org/0000-0002-2718-9996
C. W. Stubbs ⓘ https://orcid.org/0000-0003-0347-1724
A. Vikhlinin ⓘ https://orcid.org/0000-0001-8121-0234

References

Abazajian, K. N., Adshead, P., Ahmed, Z., et al. 2016, arXiv:1610.02743
Abbott, T. M. C., Abdalla, F. B., Alarcon, A., et al. 2018, PhRvD, 98, 043526
Alam, S., Ata, M., Bailey, S., et al. 2017, MNRAS, 470, 2617
Allen, S. W., Evrard, A. E., & Mantz, A. B. 2011, ARA&A, 49, 409
Applegate, D. E., von der Linden, A., Kelly, P. L., et al. 2014, MNRAS, 439, 48
Astropy Collaboration, Price-Whelan, A. M., Sipőcz, B. M., et al. 2018, AJ, 156, 123
Baxter, E. J., Raghunathan, S., Crawford, T. M., et al. 2018, MNRAS, 476, 2674
Bayliss, M. B., Ruel, J., Stubbs, C. W., et al. 2016, ApJS, 227, 3
Bender, A. N., Ade, P. A. R., Ahmed, Z., et al. 2018, Proc. SPIE, 10708, 1070803
Benson, B. A., Ade, P. A. R., Ahmed, Z., et al. 2014, Proc. SPIE, 9153, 12
Benson, B. A., de Haan, T., Dudley, J. P., et al. 2013, ApJ, 763, 147
Beutler, F., Blake, C., Colless, M., et al. 2011, MNRAS, 416, 3017
Bleem, L. E., Stalder, B., de Haan, T., et al. 2015, ApJS, 216, 27
Bocquet, S., & Carter, F. W. 2016, JOSS, 46, 1
Bocquet, S., Saro, A., Dolag, K., & Mohr, J. J. 2016, MNRAS, 456, 2361
Bocquet, S., Saro, A., Mohr, J. J., et al. 2015, ApJ, 799, 214
Bulbul, E., Chiu, I.-N., Mohr, J. J., et al. 2019, ApJ, 871, 50
Carlstrom, J. E., Ade, P. A. R., Aird, K. A., et al. 2011, PASP, 123, 568
Chiu, I., Mohr, J., McDonald, M., et al. 2016, MNRAS, 455, 258
Chiu, I., Mohr, J. J., McDonald, M., et al. 2018, MNRAS, 478, 3072
Dark Energy Survey Collaboration, Abbott, T., Abdalla, F. B., et al. 2016, MNRAS, 460, 1270
De Bernardis, F., Stevens, J. R., Hasselfield, M., et al. 2016, Proc. SPIE, 9910, 991014
de Haan, T., Benson, B. A., Bleem, L. E., et al. 2016, ApJ, 832, 95
Dietrich, J. P., Bocquet, S., Schrabback, T., et al. 2019, MNRAS, 483, 2871
Duffy, A. R., Schaye, J., Kay, S. T., & Dalla Vecchia, C. 2008, MNRAS, 390, L64
Feroz, F., Hobson, M. P., & Bridges, M. 2009, MNRAS, 398, 1601
Giannantonio, T., Fosalba, P., Cawthon, R., et al. 2016, MNRAS, 456, 3213
Gralla, M. B., Gladders, M. D., Yee, H. K. C., & Barrientos, L. F. 2011, ApJ, 734, 103
Gupta, N., Saro, A., Mohr, J. J., et al. 2017b, MNRAS, 467, 3737
Gupta, N., Saro, A., Mohr, J. J., Dolag, K., & Liu, J. 2017a, MNRAS, 469, 3069

Haiman, Z., Mohr, J. J., & Holder, G. P. 2001, ApJ, 553, 545
Heitmann, K., Bingham, D., Lawrence, E., et al. 2016, ApJ, 820, 108
Hennig, C., Mohr, J. J., Zenteno, A., et al. 2017, MNRAS, 467, 4015
Hilton, M., Hasselfield, M., Sifón, C., et al. 2018, ApJS, 235, 20
Hoekstra, H., Herbonnet, R., Muzzin, A., et al. 2015, MNRAS, 449, 685
Hunter, J. D. 2007, CSE, 9, 90
Ichiki, K., & Takada, M. 2012, PhRvD, 85, 063521
Ivezic, Z., Tyson, J. A., Abel, B., et al. 2008, ApJ, 873, 111
Jones, E., Oliphant, T., Peterson, P., et al. 2001, SciPy: Open Source Scientific Tools for Python, http://www.scipy.org/
Kaastra, J. S. 2017, A&A, 605, A51
Kaiser, N. 1986, MNRAS, 222, 323
Khullar, G., Bleem, L. E., Bayliss, M. B., et al. 2019, ApJ, 870, 7
Kravtsov, A. V., & Borgani, S. 2012, ARA&A, 50, 353
Kravtsov, A. V., Vikhlinin, A., & Nagai, D. 2006, ApJ, 650, 128
Laureijs, R., Amiaux, J., Arduini, S., et al. 2011, arXiv:1110.3193
Le Brun, A. M. C., McCarthy, I. G., Schaye, J., & Ponman, T. J. 2014, MNRAS, 441, 1270
Lin, Y., Partridge, B., Pober, J. C., et al. 2009, ApJ, 694, 992
Majumdar, S., & Mohr, J. J. 2004, ApJ, 613, 41
Mantz, A., Allen, S. W., Ebeling, H., Rapetti, D., & Drlica-Wagner, A. 2010a, MNRAS, 406, 1773
Mantz, A., Allen, S. W., Rapetti, D., & Ebeling, H. 2010b, MNRAS, 406, 1759
Mantz, A. B., Allen, S. W., Morris, R. G., et al. 2016, MNRAS, 463, 3582
Mantz, A. B., von der Linden, A., Allen, S. W., et al. 2015, MNRAS, 446, 2205
McClintock, T., Rozo, E., Becker, M. R., et al. 2019a, ApJ, 872, 53
McClintock, T., Varga, T. N., Gruen, D., et al. 2019b, MNRAS, 482, 1352
McDonald, M., Allen, S. W., Bayliss, M., et al. 2017, ApJ, 843, 28
McDonald, M., Benson, B. A., Vikhlinin, A., et al. 2013, ApJ, 774, 23
Melchior, P., Gruen, D., McClintock, T., et al. 2017, MNRAS, 469, 4899
Melin, J.-B., Bartlett, J. G., & Delabrouille, J. 2006, A&A, 459, 341
Metropolis, N., Rosenbluth, A. W., Rosenbluth, M. N., Teller, A. H., & Teller, E. 1953, JChPh, 21, 1087
Mohr, J. J., Mathiesen, B., & Evrard, A. E. 1999, ApJ, 517, 627
Peebles, P. 1980, The Large Scale Structure of the Universe (Princeton, NJ: Princeton Univ. Press)
Planck Collaboration, Ade, P. A. R., Aghanim, N., et al. 2016a, A&A, 594, A13
Planck Collaboration, Ade, P. A. R., Aghanim, N., et al. 2016b, A&A, 594, A24
Planck Collaboration, Aghanim, N., Akrami, Y., et al. 2018a, arXiv:1807.06209
Planck Collaboration, Akrami, Y., Arroja, F., et al. 2018b, arXiv:1807.06205
Rapetti, D., Blake, C., Allen, S. W., et al. 2013, MNRAS, 432, 973
Reichardt, C. L., Stalder, B., Bleem, L. E., et al. 2013, ApJ, 763, 127
Ross, A. J., Samushia, L., Howlett, C., et al. 2015, MNRAS, 449, 835
Rykoff, E. S., Rozo, E., Hollowood, D., et al. 2016, ApJS, 224, 1
Saro, A., Bocquet, S., Mohr, J., et al. 2017, MNRAS, 468, 3347
Saro, A., Bocquet, S., Rozo, E., et al. 2015, MNRAS, 454, 2305
Schrabback, T., Applegate, D., Dietrich, J. P., et al. 2018a, MNRAS, 474, 2635
Schrabback, T., Schirmer, M., van der Burg, R. F. J., et al. 2018b, A&A, 610, A85
Scolnic, D. M., Jones, D. O., Rest, A., et al. 2018, ApJ, 859, 101
Sehgal, N., Bode, P., Das, S., et al. 2010, ApJ, 709, 920
Stalder, B., Stark, A. A., Amato, S. M., et al. 2014, Proc. SPIE, 9147, 91473Y
Stern, C., Dietrich, J. P., Bocquet, S., et al. 2019, MNRAS, 485, 69
Strazzullo, V., Pannella, M., Mohr, J. J., et al. 2019, A&A, 622, A117
Sunyaev, R. A., & Zel'dovich, Y. B. 1972, CoASP, 4, 173
Tanabashi, M., Hagiwara, K., Hikasa, K., et al. 2018, PhRvD, 98, 030001
Tinker, J., Kravtsov, A. V., Klypin, A., et al. 2008, ApJ, 688, 709
Vanderlinde, K., Crawford, T. M., de Haan, T., et al. 2010, ApJ, 722, 1180
van der Walt, S., Colbert, S. C., & Varoquaux, G. 2011, CSE, 13, 22
van Uitert, E., Joachimi, B., Joudaki, S., et al. 2018, MNRAS, 476, 4662
Velliscig, M., van Daalen, M. P., Schaye, J., et al. 2014, MNRAS, 442, 2641
Vikhlinin, A., Burenin, R. A., Ebeling, H., et al. 2009a, ApJ, 692, 1033
Vikhlinin, A., Kravtsov, A. V., Burenin, R. A., et al. 2009b, ApJ, 692, 1060
von der Linden, A., Allen, M. T., Applegate, D. E., et al. 2014, MNRAS, 439, 2
Williamson, R., Benson, B. A., High, F. W., et al. 2011, ApJ, 738, 139
Wright, C. O., & Brainerd, T. G. 2000, ApJ, 534, 34
Zuntz, J., Paterno, M., Jennings, E., et al. 2015, A&C, 12, 45